# The brain's "dark energy" puzzle *upgraded*: [$^{18}$F]FDG uptake, delivery and phosphorylation, and their coupling with resting-state brain activity

Tommaso Volpi[1,2]*, John J. Lee[3], Andrei G. Vlassenko[3], Manu S. Goyal[3], Maurizio Corbetta[2,4], Alessandra Bertoldo[2,5]*

[1] Department of Radiology and Biomedical Imaging, Yale University School of Medicine, New Haven, CT 06520, USA

[2] Padova Neuroscience Center, University of Padova, 35129, Padova, Italy

[3] Neuroimaging Laboratories at the Mallinckrodt Institute of Radiology, Washington University School of Medicine, St Louis, MO 63110, USA

[4] Department of Neuroscience, University of Padova, 35121, Padova, Italy

[5] Department of Information Engineering, University of Padova, 35131, Padova, Italy

* Correspondence should be addressed to

Tommaso Volpi, Ph.D.

801 Howard Ave,

06519 New Haven, CT, USA

tommaso.volpi@yale.edu

Alessandra Bertoldo, Ph.D.

Via Gradenigo 6/B

35122 Padova, Italy

alessandra.bertoldo@unipd.it

**Running headline:** Modeling [$^{18}$F]FDG kinetics vs. fMRI

## Abstract

The brain's resting-state energy consumption is expected to be mainly driven by spontaneous activity. In our previous work, we extracted a wide range of features from resting-state fMRI (rs-fMRI), and used them to predict [$^{18}$F]FDG PET SUVR as a proxy of glucose metabolism. Here, we expanded upon our previous effort by estimating [$^{18}$F]FDG kinetic parameters according to Sokoloff's model, i.e., $K_i$ (irreversible uptake rate), $K_1$ (delivery), $k_3$ (phosphorylation), in a large healthy control group. The parameters' spatial distribution was described at a high spatial resolution. We showed that while $K_1$ is the least redundant, there are relevant differences between $K_i$ and $k_3$ (occipital cortices, cerebellum and thalamus).

Using multilevel modeling, we investigated how much of the regional variability of [$^{18}$F]FDG parameters could be explained by a combination of rs-fMRI variables only, or with the addition of cerebral blood flow (CBF) and metabolic rate of oxygen ($CMRO_2$), estimated from $^{15}$O PET data. We found that combining rs-fMRI and $CMRO_2$ led to satisfactory prediction of individual $K_i$ variance (45%). Although more difficult to describe, $K_i$ and $k_3$ were both most sensitive to local rs-fMRI variables, while $K_1$ was sensitive to $CMRO_2$. This work represents the most comprehensive assessment to date of the complex functional and metabolic underpinnings of brain glucose consumption.

**Keywords**

Brain glucose metabolism

Kinetic modeling

Microparameters

Spontaneous activity

Multilevel modeling

# Introduction

The complex interplay between the brain's metabolic rate of glucose (CMRglc) and oxygen ($CMRO_2$), cerebral blood flow (CBF), and brain activity has been the subject of investigation for a long time[1,2,3]. One of the most intriguing findings in neuroscience has been the key role that spontaneous activity plays in the context of neural metabolism. As most brain energy consumption in terms of glucose and oxygen happens during rest[4,5], one would expect some degree of coupling between indices of brain metabolism (CMRglc, $CMRO_2$), blood flow, and measures of resting-state brain activity, such as those which can be derived from resting-state blood oxygen level dependent (BOLD) functional MRI (rs-fMRI)[6]. A moderate-to-strong association between resting-state CMRglc, $CMRO_2$ and CBF has been postulated, and demonstrated by PET studies using [$^{18}$F]FDG, [$^{15}$O]$H_2O$, and [$^{15}$O]$O_2$ tracers[7,8]. A growing number of studies have also tested the coupling between brain glucose metabolism and features obtained from rs-fMRI, detecting complex associations, with stronger coupling of glucose metabolism with local indices of BOLD activity and synchronization, and marked between-individual variability in the strength of the association[8,9,10,11,12,13].

In our previous work[13], we explored the link between the spatial topography of glucose metabolism, as measured via [$^{18}$F]FDG PET, and a variety of rs-fMRI measures in the healthy brain, attempting to capture the complexity of brain metabolism through a multifaceted assessment of spontaneous activity. As in many other research works[10,11,12], we employed a semi-quantitative measure of [$^{18}$F]FDG uptake, i.e., the standardized uptake value ratio (SUVR). While this was validated to be a reliable index of glucose consumption in the healthy brain, it gives a simplified view of the physiological events that can be tracked by [$^{18}$F]FDG PET: this

tracer, if combined with compartment modeling, can be used to separately estimate tracer delivery ($K_1$) across the blood-brain barrier (BBB) mediated by glucose transporters (GLUT1, GLUT3)[14] , clearance into the venous blood ($k_2$), and phosphorylation rate by hexokinase ($k_3$). These microparameters ($K_1$, $k_2$, $k_3$) complement and enrich the picture given by the irreversible uptake rate of [$^{18}$F]FDG ($K_i = K_1k_3/(k_2+k_3)$), which is a composite macroparameter[15,16]. $K_1$ is an expression of both CBF and the tracer's extraction fraction $E$ ($K_1 = E \cdot$ CBF), and thus BBB permeability[17]. $k_3$ represents glucose phosphorylation, which is the rate limiting step for glucose utilization, and thus of particular physiological and pathological relevance[18,19]; $k_3$ should be strongly related to $K_i$, making $K_i$ a good proxy of glucose phosphorylation events, but there are regions where removing the impact of delivery may prove relevant. The spatial distribution of the microparameters was investigated for the first time in the 1980's[20], and in few other works[19,21], but a more fine-grained evaluation is warranted, considering lingering questions in the fields of neural metabolism and spontaneous activity.

In this work, we focused on fully exploiting the physiological information that can be extracted from dynamic [$^{18}$F]FDG PET data in a large dataset of healthy controls (n = 47). This was intended to expand upon our previous study, where, using two datasets, we showed that rs-fMRI measures can explain a moderate portion of regional metabolic variability (as described by SUVR), mainly driven by local rs-fMRI features[13]. However, a significant amount of variance remained unexplained. Here, we evaluated the spatial distribution of [$^{18}$F]FDG $K_i$, $K_1$, and $k_3$, and related them to a multitude of potential rs-fMRI predictors (**Table 1**), divided into four pools[13]: 1) *signal*, 2) hemodynamic response function (*HRF*)[22], 3) static functional connectivity (*sFC*)[23], 4) time-varying functional connectivity (*tvFC*)[24]. We also related $K_i$, $K_1$, $k_3$ to CBF and $CMRO_2$,

as estimated from [$^{15}$O]$H_2O$, [$^{15}$O]$O_2$ PET, which more directly reflect hemodynamics and oxidative metabolism[25]. The main aims driving our analyses were:

1) assessing the spatial distribution of [$^{18}$F]FDG $K_i$, $K_1$, $k_3$ across brain regions in healthy individuals, with particular focus on $K_1$ and $k_3$, assuming they would provide unique information;
2) evaluating how much the individual-level spatial coupling between rs-fMRI measures (as proxies for the properties of spontaneous brain activity) and [$^{18}$F]FDG PET changes when considering macro- and microparameters instead of SUVR, employing multivariable mixed-effects modeling (MEM), and the same functional features identified by feature selection in our SUVR model[13], to test their reproducibility and generalizability;
3) evaluating the role of CBF and $CMRO_2$ when added to the fMRI-based description of [$^{18}$F]FDG kinetic parameters, hypothesizing that only through this more comprehensive assessment of the brain's functional properties we would reach a somewhat satisfactory description of glucose metabolism in its entirety.

The main scheme of the analysis is reported in **Figure 1**.

# Materials and Methods

*Participants and imaging protocols*

The dataset includes 47 healthy participants (22 F; 57.4 ± 14.8 years) from the Adult Metabolism & Brain Resilience study[26]. Imaging procedures were approved by Human Research Protection Office and Radioactive Drug Research Committee at Washington University in Saint Louis. T1w and rs-fMRI (TR/TE=800/33 ms, 2.4 mm isotropic, multiband factor 6) were acquired on a Siemens Prisma$^{fit}$ scanner. Eyes-closed [$^{18}$F]FDG (60 min), [$^{15}$O]$H_2O$ (3 min), [$^{15}$O]$O_2$ (3 min) PET acquisitions were performed on a Siemens ECAT EXACT HR+.

All studies were conducted according to the principles outlined in the Declaration of Helsinki. All participants provided written consent. Details are reported in **Supplementary Methods** and in [26].

*PET kinetic modeling*

Dynamic [$^{18}$F]FDG PET data were motion-corrected[27]. To perform kinetic modeling, an image-derived input function (IDIF) was extracted from dynamic PET data using a semi-automatic pipeline[28] including 1) carotid artery segmentation; 2) selection of "hot voxels" within the mask; 3) parametric clustering[29] to derive the raw IDIF; 4) IDIF model fitting; 5) Chen's spillover correction[30] using three late venous samples. Voxel-wise estimation of Sokoloff's model parameters (irreversible two-tissue compartment model) was performed using a variational Bayesian approach[31]: k-means clustering was applied to dynamic data to extract 6 gray matter (GM) and 5 white matter (WM) clusters (based on T1w tissue segmentations), then weighted nonlinear least squares was used to estimate Sokoloff's model parameters at the cluster level, and

finally voxel-wise estimation was performed using Variational Bayesian inference based on prior distributions derived from cluster-wise estimates[32]. Parametric maps of $K_1$ [mL/cm$^3$/min] (tracer inflow), $k_2$ [min$^{-1}$] (efflux), $k_3$ [min$^{-1}$] (phosphorylation), $V_b$ [%] (blood volume fraction) were obtained for each individual. The parametric map of $K_i$ [mL/cm$^3$/min] (irreversible tracer uptake) was obtained as $K_i = K_1k_3/(k_2+k_3)$. The group-average maps of $K_i$, $K_1$, $k_3$ are reported in **Figure 2**, while $k_2$ and $V_b$ are reported in **Figure S1**.

Dynamic [$^{15}$O]$H_2O$ PET was quantified with a one-tissue compartment model[33] and a model-based input function[34] to estimate CBF. Dynamic [$^{15}$O]$O_2$ PET was used to estimate $CMRO_2$, employing a reference-tissue approach[35]. The group-average maps of CBF and $CMRO_2$ are reported in **Figure S1**.

All parametric maps were parcellated into 216 regions (Schaefer atlas[36], supplemented by 16 subcortical regions[37]), by averaging over voxels within the GM segmentation (probability > 0.8 of belonging to GM).

We did not perform partial volume correction on PET data: using the GM tissue segmentation and avoiding spatial smoothing of PET data during processing minimizes partial volume effects (PVE)[38], as also suggested in recent work[39]. Moreover, there is no gold standard for partial volume correction, particularly in dynamic PET studies, as this procedure is known to affect kinetic modeling accuracy and potentially alter spatial metabolic patterns[40].

Details are reported in **Supplementary Methods**.

*Resting-state fMRI processing and feature extraction*

Preprocessing of rs-fMRI included slice-timing correction, nuisance regression[41,42], high-pass filtering (cut-off = 0.008 Hz). Additional motion correction was adapted to the rs-fMRI features

(i.e., despiking for tvFC, HRF, and other time-varying measures, and volume censoring for sFC and static measures[43]). The BOLD signals were also parcellated into 216 regions (GM-masked). As in [13], fifty rs-fMRI features were obtained in each participant. The extracted features were chosen to describe different aspects of the BOLD 1) *signal*, 2) *HRF*, 3) *sFC*, 4) *tvFC* (**Table 1**). The *signal* pool (1) relates to the basic statistics of the BOLD time series (temporal median, variance, skewness), its complexity/entropy[44], its low-frequency fluctuations (*ALFF*)[45], local coherence (*ReHo*)[46] and high-amplitude events (*peaks-BOLD*). The *HRF* pool (2) relates to the HRF[22], which links the BOLD signal to neural activity[47], and includes the HRF peak amplitude (a potential proxy for CBF[48]), and the correlations between HRF time series of different regions, which we introduced in [13] to describe "purely vascular" networks, summarized at the region level by means of graph properties, for correspondence with traditional FC studies[49]. In the *sFC* pool (3) the same graph metrics are employed to characterize sFC, i.e., FC calculated across the entire fMRI scan. The *tvFC* pool (4) describes the temporal variability of graph metrics across sliding windows[24] for each brain region. sFC and tvFC were characterized both as the correlation between BOLD signal *magnitudes*, and as the coherence of their *phases*[50]. This wide range of functional metrics were selected to represent the majority of known properties of the rs-fMRI signal and its FC. See **Supplementary Methods** for details.

*The spatial distribution of [$^{18}$F]FDG kinetic parameters and their relationships*

To investigate the spatial distribution and regional variability of $K_i$, $K_1$ and $k_3$, the group-average ROI values were calculated. The $K_i$, $K_1$ and $k_3$ ROI values were grouped into Schaefer's 17 functional networks[36]. The top and bottom 20% values of each kinetic parameter were identified as 'high' and 'low', and visualized. Across-*region* Pearson's correlations ($p<0.05$) between the

three group-average parameter vectors were computed. Linear regression models ($K_i$ as predictor, $K_1$ and $k_3$ as separate outcomes) were estimated and their weighted residuals visualized to assess the presence of regional mismatches between parameters.

*Bivariate associations between [$^{18}$F]FDG kinetic parameters and functional features*

The bivariate spatial relationship between [$^{18}$F]FDG kinetic parameters and A) rs-fMRI properties, B) CBF and $CMRO_2$, was assessed at group level, taking the region-wise mean values across individuals for each of the features. After testing for Gaussianity ($p>0.05$, Shapiro-Wilk test[51]), the bivariate associations across ROIs were evaluated via Pearson's correlation ($p<0.05$). Differences between [$^{18}$F]FDG parameters in their spatial correlation with A) rs-fMRI properties, B) CBF and $CMRO_2$ were tested using Steiger's z-test for dependent correlations with one variable in common ($p<0.05$). The average and variability (mean ± SD) of the squared values of [$^{18}$F]FDG vs. rs-fMRI spatial correlations ($R^2$) were computed, as indices of the overall strength of functional-metabolic spatial association across fMRI variables. Differences among [$^{18}$F]FDG parameters (factor 1) and groups of rs-fMRI features (factor 2) in the strength of [$^{18}$F]FDG-fMRI association ($R^2$) were assessed using a two-way analysis of variance (ANOVA) with unbalanced design, with [$^{18}$F]FDG parameters as first factor (3 levels: $K_i$, $K_1$, $k_3$), and groups of rs-fMRI features as second factor (4 levels: signal, HRF, sFC, tvFC). Statistical differences between pairs of means were determined using Tukey-Kramer's multiple comparison test.

The spatial heterogeneity in the [$^{18}$F]FDG-fMRI relationship was probed by assessing correlations iteratively across clusters of regions with increasingly high or low $K_i$, $K_1$ or $k_3$. The threshold levels were determined by considering linearly *increasing* percentiles ($1^{st}$ to $85^{th}$) of the [$^{18}$F]FDG parameter distribution over all regions, and linearly *decreasing* $K_i$, $K_1$ or $k_3$ percentiles

($100^{th}$ to $15^{th}$). For each threshold level (i.e., group of chosen regions), Pearson's correlations between [$^{18}$F]FDG parameters and all A) rs-fMRI features, B) CBF and $CMRO_2$ were calculated. The type of bivariate relationship between [$^{18}$F]FDG and rs-fMRI properties was also tested by comparing three models, i.e., 1) linear, 2) mono-exponential, 3) power law. Model selection was performed using the residual sum of squares (RSS)[53]. See [13] and **Supplementary Methods** for details.

*Multivariable modeling of the functional-metabolic relationship at group level*

At group-average level, we used a multilinear regression approach to assess how much of the group-average [$^{18}$F]FDG $K_i$, $K_1$ and $k_3$ could be explained by a linear combination of predictors, i.e., multiple rs-fMRI variables and/or CBF, $CMRO_2$. Predictors and outcome were centered and scaled by their standard deviation (SD) across brain regions, and log-transformed, as in [13], to account for nonlinearities (**Supplementary Results**).

Rather than performing a new feature selection for each of the kinetic parameters, we tested whether the predictors selected for SUVR in [13] would generalize to $K_i$, $K_1$ and $k_3$: specifically, we considered both the full SUVR model (9-parameter model, 9p) and its more parsimonious version (3-parameter model, 3p)[13]. The models' coefficients were re-estimated. The tested models were evaluated in terms of number of predictors, adjusted R-squared ($R^2_{adj}$), and estimate precision (i.e., percent standard error divided by estimated value, %SE). An "adapted" version of the 9p model was generated, by excluding predictors whose estimates had %SE>100%. To assess the presence of multicollinearity, we also examined the Pearson's correlations among predictors, the condition number $\kappa(X)$ of the selected features, and variance inflation factors[54].

As a second step, the addition of CBF or $CMRO_2$ to the selected fMRI-based models was evaluated in terms of goodness of fit ($R^2_{adj}$) and %SE.

*Full hierarchical modeling of [$^{18}$F]FDG kinetic parameters using functional predictors*

As in our previous work[13], full *multilevel* population modeling (MEM) was implemented to characterize in a single stage both fixed effects $\theta$ and random effects $\eta$ contributing to the relationship between [$^{18}$F]FDG parameters and the selected functional variables[56]. The *individual*-level model is:

$$y_i = F_i(X_i, \psi_i)$$

$$z_i = y_i + v_i$$

with $y_i$ as the $K_1$, $K_1$ or $k_3$ prediction for the $i^{th}$ individual ($i = 1, \dots, m$), which is a function of $X_i$ (the fixed-effects design matrix), and of parameters $\psi_i$ to be estimated; $z_i$ is the vector of $K_1$, $K_1$ or $k_3$, and $v_i$ is the *within-individual variability*, assumed to be normally distributed with zero mean and variance $\sigma_i^2$. The *population*-level model describes $\psi_i$ combining the population parameters $\theta$ and the random variability of individual parameters around the population mean $\eta_i$:

$$\psi_i = \theta + \eta_i$$

$$\eta_i \sim N(0, \Omega)$$

where $\eta_i$ is normally distributed with zero mean, independent across individuals and with covariance matrix $\Omega$ (assumed to be full). The features selected in the previous step were included in the first-level model, i.e., either rs-fMRI features only, or including CBF or $CMRO_2$, after within-individual z-scoring. The overall and individual multilevel model $R^2_{adj}$ were

evaluated, considering the pooled data of all participants ($R^2_{pooled}$) and the single individual data ($R^2_i$), respectively. The mean (*avg. wres*) and SD of the residual unexplained variability were evaluated. The areas with higher positive ([0.5;1.5]) or negative ([-1.5;-0.5]) avg. wres were visualized to highlight where the model under- or over-estimates the outcome variable. When participant-specific covariates were available, i.e., age ([years]), sex, height ([m]), weight ([kg]), body-mass index (BMI, [$kg/m^2$]), body-surface area (BSA, [$m^2$]), insulin plasma levels ([mIU/L]), Pearson's correlations ($p<0.05$) relating $R^2_i$ and these covariates were calculated. For more details, see **Supplementary Methods**.

# Results

*The spatial distribution of [$^{18}$F]FDG uptake, delivery and phosphorylation rates*

First, the kinetic model parameters estimated from [$^{18}$F]FDG dynamic data, i.e., $K_i$, $K_1$ and $k_3$, were evaluated (**Figure 2**). The choice to describe their spatial distribution and regional variability across the selected brain parcellation was motivated by the importance to understand the unique information they provide. The region-wise interindividual variability of [$^{18}$F]FDG parameters is reported in **Figure S2**.

The parcels representing the top and bottom 20% values of the average regional distribution of $K_i$, $K_1$ and $k_3$ were examined (**Figure 3**). Both $K_i$ and $k_3$ had many top nodes in lateral prefrontal areas, parietal and posteromedial cortex, while $K_1$ had mainly a strong distribution of top posteromedial nodes including posterior cingulate and occipital areas, but also in medial sensorimotor regions. When looking at the bottom nodes, limbic areas, both at the level of the temporal poles and anterior cingulate cortex, were represented for all three parameters; however, $k_3$ had strong presence of bottom nodes in the visual cortex, which is missing in $K_i$, and $K_1$ presented additional low nodes in the frontal cortex (both motor and cognitive areas) and insula.

When focusing on the subcortex, we again found a similar pattern for $K_i$ and $k_3$, with the putamen as a top parcel, and cerebellum as a bottom one. However, the differences emerge for the caudate, which is a bottom node only for $K_i$, and for the thalamus, which is low only for $k_3$. In the case of $K_1$, the putamen is again a top parcel, and the caudate is a bottom node like in the case of $K_i$; the thalamus and cerebellum are instead amongst the top regions.

Looking at [$^{18}$F]FDG kinetic parameters with a perspective based on functional brain networks (**Figure 3**, boxplots) does not seem to capture a clear ranking, at least for $K_i$ and $k_3$, consistent with our observations for SUVR[12]. $K_1$ is clearly highly represented in visual areas.

The spatial correlations (Pearson's r) between the group-average parameters (**Figure S3**) across the regions of the chosen parcellation are as follows: $K_i$ vs. $K_1$: r = 0.56 ($p < 10^{-18}$); $K_i$ vs. $k_3$: r = 0.88 ($p < 10^{-70}$); $K_1$ vs. $k_3$: r = 0.19 (p = 0.006).

To better quantify the extent of the regional mismatch between $K_i$ and each microparameter, we plotted the weighted residuals of the two linear regression models ($K_1$ or $k_3$ as outcome, $K_i$ as predictor), by showing only the highest positive or negative residual values, to emphasize the regions where $K_i$ fails to predict $K_1$ or $k_3$ well (**Figure S4**). $K_1$ has higher-than-expected values in posteromedial areas, while it fails to follow the high $K_i$ values of the lateral frontal areas and caudate nuclei. As for $k_3$, we find markedly lower values in visual cortex and cerebellum than expected by $K_i$, but also in thalamus; instead $k_3$ relatively exceeds $K_i$ mainly in the caudate nuclei, but also in insular and lateral cortical areas.

Across-individual region-wise correlations between [$^{18}$F]FDG parameters are reported in **Figure S5**.

*Bivariate associations with functional features*

As in our previous work[13], we extracted 50 rs-fMRI variables at the individual level, and subdivided them into 4 *a priori*-defined pools: 1) *signal*, 2) *HRF*, 3) *sFC*, 4) *tvFC* (**Table 1**).

The correlation matrix between all available functional features, i.e., A) the 50 rs-fMRI features, B) CBF and $CMRO_2$, at group-average level are reported in **Figure S6**.

The Pearson's correlations between group-average [$^{18}$F]FDG parameters and rs-fMRI features are presented in **Figure 4** (individual-level results in **Figure S7**).

In the signal pool, moderate-to-strong positive or negative correlations are present for $K_i$ and $k_3$ with features related to rs-fMRI "signal" features (*ALFF*, *ReHo* and its temporal variability, and *peaks-BOLD*), while $K_1$ shows weaker coupling (not significant, 2-way ANOVA). Notably, *peak-HRF*, which represents blood flow-related information, is significantly, though weakly correlated with $K_1$ and $K_i$, but not with $k_3$. Moreover, HRF network features are only related to $K_1$. Interestingly, all sFC measures display significant associations with $K_1$, but not with $k_3$, while $K_i$ presents a mixed situation. Finally, in the case of the tvFC pool, the pattern of correlations is similar for the three [$^{18}$F]FDG parameters, albeit with stronger negative correlations for $K_i$ (not significant, 2-way ANOVA). When assessing the squared values of correlations with rs-fMRI features, $K_i$ and $K_1$ have similar magnitudes, while $k_3$ has significantly lower correlations than $K_i$ (Tukey-Kramer test, $p < 0.01$).

CBF is correlated with $K_i$ ($r = 0.43$, $p < 10^{-10}$), $K_1$ ($r = 0.38$, $p < 10^{-8}$), and $k_3$ ($r = 0.25$, $p < 10^{-3}$); $CMRO_2$ has stronger associations than CBF with all parameters (Steiger's test, $p < 0.05$), i.e., $K_i$ ($r = 0.60$, $p < 10^{-22}$), $K_1$ ($r = 0.61$, $p < 10^{-22}$), and $k_3$ ($r = 0.32$, $p < 10^{-5}$).

Building on our finding that the SUVR-fMRI coupling is stronger in lower SUVR nodes[13], we reassessed [$^{18}$F]FDG-fMRI Pearson's correlations ($p < 0.05$) across nodes selected according to linearly increasing as well as decreasing percentiles of each [$^{18}$F]FDG parameter's distribution (**Figure S8**). Despite some differences between parameters, we confirmed that nonlinearities exist in the spatial relationship between [$^{18}$F]FDG parameters and rs-fMRI features across brain regions, and that functional-metabolic associations are overall stronger in low-metabolism brain

regions. Notably, sFC features have the most marked nonlinear associations with [$^{18}$F]FDG parameters, especially $K_i$ and $k_3$ (**Figure S9**).

*The fMRI-only models of [$^{18}$F]FDG kinetic parameters*

We then evaluated whether the combination of rs-fMRI features we had chosen for SUVR[13] (both 9p and 3p models) could explain the regional variability of $K_i$, $K_1$ and $k_3$. The 9p model included 1) approximate entropy of BOLD (*ApEn-BOLD*), 2) range ApEn-BOLD (*rApEn-BOLD*), 3) *ReHo*, 4) coefficient of variation of ReHo (*CV-ReHo*), 5) *peaks-BOLD*, 6) local efficiency of HRF network (*hrf-LE*), 7) sFC betweenness centrality (*s-BC*), 8) median of leading eigenvectors of BOLD phase coherence (*med-LEig*), 9) coefficient of variation of betweenness centrality (*CV-BC*). Features 1-5 are from the signal pool, 6 is from the HRF pool, 7-8 from the sFC pool, and 9 from the tvFC pool (**Table 1**). The 3p model included 1) *ReHo*, 2) *CV-ReHo*, 3) *CV-BC*.

For group-average $K_i$, the 9p model had an $R^2_{adj}$ of 0.68 (3p model: 0.60); such performance is very similar to group-average SUVR in our previous work (9p model: 0.69, 3p model: 0.59)[13]. For group-average $K_1$, the 9p model had an $R^2_{adj}$ of 0.34 (3p model: 0.23). For group-average $k_3$, the 9p model had an $R^2_{adj}$ of 0.5 (3p model: 0.44).

An adapted version of the 9p model was generated for each [$^{18}$F]FDG parameter by removing features whose estimates had unacceptable precision (%SE>100%). This led to a 6-parameter model for $K_i$ (*ApEn-BOLD*, *rApEn-BOLD*, *ReHo*, *CV-ReHo*, *med-LEig*, *CV-BC*; $R^2_{adj}$ = 0.69), an 8-parameter model for $K_1$ (*rApEn-BOLD*, *ReHo*, *CV-ReHo*, *peaks-BOLD*, *hrf-LE*, *s-BC*, *med-LEig*, *CV-BC*; $R^2_{adj}$ = 0.34), a 5-parameter model for $k_3$ (*rApEn-BOLD*, *ReHo*, *peaks-BOLD*, *s-BC*, *med-LEig*; $R^2_{adj}$ = 0.5).

The full MEM approach (**Figure 5**) with the features selected in the previous step (adapted 9p model) explained a significant proportion of individual-level variability in the spatial distribution of $K_i$ ($R^2_{pooled}$ = 0.35), but less so in the case of $K_1$ ($R^2_{pooled}$ = 0.14) and $k_3$ ($R^2_{pooled}$ = 0.21). The predictor *peaks-BOLD* was removed from the $K_1$ model as its fixed effect estimate was not significantly different from zero. *ReHo* was confirmed as the most important explanatory parameter for $K_i$ and $k_3$ in particular (**Figure 5A**).

At the group-average level, *ReHo* explains a large proportion of variance for both $K_i$ ($R^2$ = 0.552) and $k_3$ ($R^2$ = 0.407). When recomputing the MEM estimates using only *ReHo* as a predictor, we obtained a $R^2_{pooled}$ of 0.30 for $K_i$ and 0.16 for $k_3$ (0.08 for $K_1$): this demonstrated that *ReHo* was responsible for the majority of the explained variance in the multivariable $K_i$ and $k_3$ models. Of note, in all three cases the most important parameter (with the highest associated weight) comes from the pool of signal and local rs-fMRI features.

When examining the *avg. wres* (**Figure 5C**), a marked resemblance to the top and bottom regions of each parameter (see **Figure 2**) was still present, implying that the high and low "outlier" [$^{18}$F]FDG nodes were not adequately interpreted by the chosen rs-fMRI features. This is true especially for $K_1$, which shows high residual values in posteromedial cortex and cerebellum, but also for $K_i$ and $k_3$, with high values in the putamen and low in the cerebellum.

Our finding of high between-individual variability in multilevel model $R^2$ values for SUVR[13] was confirmed here for $K_i$, $K_1$ and $k_3$ (**Figure 5B**). The individual $R^2_i$ of $K_i$ and $k_3$ do not correlate significantly with participants' age or any of the peripheral metabolic information ($p > 0.05$). However, the $R^2_i$ for $K_1$ show evidence of sex difference, i.e., higher $K_1$ $R^2_i$ for women (t-test, $p < 0.01$). Moreover, a negative relationship emerged between $R^2_i$ of $K_1$ and BSA ($r = -0.30$, $p = 0.04$) and insulin levels ($r = -0.35$, $p = 0.03$) (**Figure S10**).

*Adding CBF, $CMRO_2$ to models of [$^{18}$F]FDG parameters*

We then verified the impact of including CBF or $CMRO_2$ along with rs-fMRI features into this multivariable modeling framework to describe the spatial distribution of [$^{18}$F]FDG parameters. The spatial correlation between group-average CBF and $CMRO_2$ is $r = 0.9$ ($p < 10^{-77}$), which is why we avoided including both parameters in the same model.

At group-average level, the addition of CBF to the adapted 9p model increased the $R^2_{adj}$ from 0.68 to 0.78 for $K_i$, the $R^2_{adj}$ from 0.34 to 0.41 for $K_1$, and the $R^2_{adj}$ from 0.5 to 0.55 for $k_3$. The inclusion of $CMRO_2$, on the other hand, increases the $R^2_{adj}$ from 0.68 to 0.77 for $K_i$, the $R^2_{adj}$ from 0.34 to 0.52 for $K_1$, and the $R^2_{adj}$ from 0.5 to 0.51 for $k_3$. Parameter precision remains within an acceptable range (%SE < 100%). Overall, CBF and $CMRO_2$ led to similar improvements in the $K_i$ and $k_3$ models (moderate and minor, respectively), but $CMRO_2$ importantly improved the $K_1$ model (almost 20% of the variance).

We then assessed how these improvements impact the full MEM framework. Notably, the addition of $CMRO_2$ to the adapted 9p models led to a marked increase in explained variance of the individual-level data for $K_i$ ($R^2_{pooled}$: from 0.35 to 0.46) and $K_1$ ($R^2_{pooled}$: from 0.14 to 0.28), with minor improvement for $k_3$ ($R^2_{pooled}$: from 0.21 to 0.24). For comparison, if only $CMRO_2$ is used as a predictor, we obtained a $R^2_{pooled}$ of 0.22 for $K_i$, and 0.18 for $K_1$. The individual model $R^2_i$ can be visualized in **Figure 6B**, and the improvements appreciated by comparison with **Figure 5B**. When assessing the fixed effects, *ReHo* and $CMRO_2$ had the highest weights in the $K_i$ model, while in the $k_3$ model, *ReHo* was the most relevant parameter, as was $CMRO_2$ in the $K_1$ model (**Figure 6A**). When examining the *avg. wres.* (**Figure 6C**), we can see the improvement in explanatory power with respect to the fMRI-only models (**Figure 5C**). This is true both for $K_i$,

which no longer shows high residual values in posteromedial cortex, and for $K_1$, with improvements in posterior DMN, thalamus and putamen.

Adding CBF led to an increase in explained variance of the individual-level data for $K_i$ ($R^2_{pooled}$ = 0.45), similar to $CMRO_2$, while the benefit was lower for $K_1$ ($R^2_{pooled}$ = 0.23) and $k_3$ ($R^2_{pooled}$ = 0.25), as anticipated by the group-average modeling results.

Of note, when adding $CMRO_2$ and CBF, a negative relationship between $R^2_i$ of $K_1$ and insulin levels was still present (r = -0.41, p = 0.01).

When minimizing the number of predictor variables, i.e., only *ReHo* and $CMRO_2$, we reached a $R^2_{pooled}$ of 0.43 for $K_i$, and 0.21 for $k_3$; using only *ReHo* and CBF, the $R^2_{pooled}$ of $K_i$ is 0.42, and the $R^2$ of $k_3$ is 0.20.

## Discussion

In this work, we assessed the regional distribution of [$^{18}$F]FDG kinetic parameters ($K_i$, $K_1$ and $k_3$), disentangling the early steps of brain glucose metabolism (delivery vs. phosphorylation by hexokinase) for the first time at high spatial resolution. We then investigated how well these kinetic parameters can be described by a combination of features derived from rs-fMRI and expected to represent spontaneous brain activity. As in our previous work[13], we hypothesized that a combination of many facets of spontaneous BOLD activity would be able to collectively explain (part of) glucose metabolic variance. Finally, to overcome potential limitations in rs-fMRI features' explanatory power, we included more direct measures of hemodynamics and metabolism, i.e., regional blood flow (CBF) and oxygen consumption ($CMRO_2$). We again took advantage of the multilevel modeling framework to fully account for between-individual variability in the investigated relationships. This study thus expands upon our effort[13] to address the complexity of brain glucose metabolism[57], which involves both oxidative and glycolytic components supporting numerous cellular processes (protein synthesis, protein modification, cell signaling, housekeeping duties, postsynaptic potentials, vesicle recycling etc.)[57,58], with the exact partitioning of the brain's energy budget into these processes still an object of ongoing research[4]. To better comprehend these complex biological mechanism, we used kinetic modeling to estimate [$^{18}$F]FDG parameters at high spatial resolution (i.e., voxels, then grouped into 216 ROIs), in particular the microparameters ($K_1$ and $k_3$). While SUVR (which can be obtained from a short static scan, with no arterial sampling) can be a good proxy measure of $K_i$, it is both relative and semi-quantitative, and susceptible to multiple technical and physiological biases[59,60]. We have shown here that $K_i$, i.e., the total [$^{18}$F]FDG uptake rate constant, is a good proxy for $k_3$,

i.e., the rate of phosphorylation events, with group-average $K_i$ and $k_3$ maps being highly spatially correlated. This high level of matching is expected, since [$^{18}$F]FDG does not display flow limitation ($k_3$ is, on average, low, and smaller than $k_2$)[61]. However, operating at a higher level of detail than before, we have also found that $k_3$ relatively "underestimates" $K_i$ in visual cortex, cerebellum, and thalamus, and "overestimates" $K_i$ in the caudate, insular and frontoparietal cortex (as shown by residuals). In such areas, especially those where $k_3$ "underestimates" $K_i$, tracer delivery (influx $K_1$, and, less importantly, efflux $k_2$) seems to play a relevant role, making $K_i$ a biased predictor of the glucose phosphorylation events. This stresses how quantifying microparameters is not redundant, albeit more technically challenging.

When we moved to assess the explanatory power of rs-fMRI features for the parameters related to glucose utilization, i.e., $K_i$ and $k_3$, we found overall similar results to our findings based on SUVR[13]: a) variable degrees of spatial association with rs-fMRI variables were present, with strongest match for signal-related, local features; b) evidence of nonlinearity in this association (especially for sFC features); c) the top and bottom regions for $K_i$ and $k_3$ difficult to describe using only rs-fMRI features; d) marked between-individual variability in the association strength. Among these findings, the most relevant is the fact that *ReHo*, i.e., the local synchronization of the BOLD signal, emerged again as the rs-fMRI variable having the strongest spatial match with [$^{18}$F]FDG $K_i$ and $k_3$. *ReHo* alone was capable of explaining 55% of $K_i$ variance at group level, and 30% on individual data (as for SUVR); for $k_3$, it explained 40% of group-level variance (18% at individual level). This confirms the moderate-to-strong spatial coupling between glucose metabolism, here assessed through full kinetic modeling, and measures of *local* BOLD signal coherence. It remains to be seen whether this mostly reflects the metabolic demand of brain *structure*, or rather of spontaneous *activity* levels[13].

The next step was to include more direct hemodynamic (CBF) and metabolic ($CMRO_2$) measures into this equation, which allow to describe blood flow and oxidative vs. non-oxidative brain metabolism. Notably, the strength of spatial association between these parameters and [$^{18}$F]FDG $K_i$ or $k_3$ was somewhat weaker than expected, especially for CBF[8,62]. However, recent literature reports a moderate (r = 0.56), nonlinear association between fully quantitative CMRglc and CBF estimates (higher-than-expected CBF in thalamus, cerebellum and medial temporal lobe[39]), which is in line with our findings. Methodological differences in how these parameters are estimated in different studies (absolute vs. relative, and semiquantitative vs. quantitative) might have relevant impact. Nevertheless, the combination of fMRI variables (*ReHo* in particular) and CBF or $CMRO_2$ led to satisfactory $K_i$ spatial description (nearly 80% of group-level, 45% of individual-level variance), with marked amelioration of the pattern of the residuals, especially in areas with the strongest positive "outliers" (posterior cingulum). This confirms our hypothesis: the combination of direct hemodynamic and metabolic information, as provided by CBF and $CMRO_2$, with information on spontaneous brain activity provided by the BOLD signal explains a large portion of individual-level variance (nearly half) in glucose metabolism (as expressed by $K_i$). On the other hand, the difficulty in reaching a fully satisfactory description, particularly for $k_3$ spatial variability (18% at individual level), despite the high number of available features (rs-fMRI, CBF, $CMRO_2$), calls for more extensive exploration, potentially looking into other measures, both structural/molecular, such as the spatial distribution of hexokinase isoforms (HK1, HK2), or activity-related, e.g., from electrophysiological signals, which could also help better understand the metabolic role played by *ReHo*, whose biological underpinnings are still unclear.

A separate discussion is warranted for [$^{18}$F]FDG delivery ($K_1$), which has the most peculiar and interesting spatial distribution, with a markedly posterior pattern (visual cortex, cerebellum, thalamus as "top" parcels), and apparent even in the earliest studies with low-resolution PET cameras[20]. As mentioned in these prior studies[20], one might be tempted to consider vascular territory effects (i.e., the highest $K_1$ values largely encompass the posterior circulation), but this does not seem to be a satisfactory explanation, not least because the anterior circulation also provides blood flow to the posterior cerebral territories via the posterior communicating arteries. Notably, the blood volume contribution to the PET signal ($V_b$), which may differ among vascular territories due to heterogeneous blood velocity, is accounted for during model fitting. Alternatively, some relationship may exist between $K_1$ and the expression of different isoforms of glucose transporters (GLUT1 and GLUT3, but also SGLT transporters)[14]. Intriguingly, it is also worth noting that although measures of oxygen extraction fraction (OEF) are largely similar throughout the brain, several studies have noted higher OEF in the occipital cortex[63,64].

When relating $K_1$ to BOLD measures, it was the only [$^{18}$F]FDG parameter that had significant bivariate associations with most HRF and sFC features. The relatively strong coupling of HRF and large-scale FC network features with $K_1$ seems to confirm that blood flow and BBB permeability information (of which $K_1$ is a combination) are important contributors to the rs-fMRI signal[48], and potentially more linked to large-scale FC than glucose metabolism itself. However, BOLD-based information alone did not provide sufficient explanation of the spatial distribution of $K_1$ (group-average $R^2 \sim 0.35$, pooled $R^2 \sim 0.15$). Importantly, the inclusion of $CMRO_2$ in the fMRI-based models markedly increased explained variance of the individual $K_1$ data (pooled $R^2 \sim 0.3$), improving the pattern of the residuals. This finding is consistent with previous reports separately describing the posteromedial spatial distributions of [$^{18}$F]FDG $K_1$[21]

and $CMRO_2$[62] (and OEF). Notably, some key differences between the two parameters can also be identified: the cerebellum, in particular, is a "hotspot" for $K_1$ only; its peculiar structural and physiological characteristics might explain its high [$^{18}$F]FDG delivery, including its different glia-to-neuron ratio[65], density and type of glucose transporters, different lumped constant[14], higher $E$ and PS product[66] etc. Of note, CBF was not as effective as a predictor for $K_1$; this is, however, not surprising, since [$^{18}$F]FDG is not a highly extracted tracer (average $E < 20\%$)[66], and $K_1$ and CBF are nonlinearly related ($K_1 = CBF \cdot E = CBF \cdot \left(1 - e^{-\frac{PS}{CBF}}\right)$ (PS as the permeability-surface product), with $E$ having some regional heterogeneity[66]. From a physiological standpoint, the strong association between the delivery of glucose ($K_1$) and the delivery and consumption of oxygen ($CMRO_2$), is interesting and highlights $K_1$'s metabolic relevance. Further indicators of the metabolic role played by $K_1$ are the correlations between the strength of its coupling with BOLD and/or $CMRO_2$, and peripheral metabolism. Only the $K_1$-BOLD and $K_1$-$CMRO_2$ coupling strengths (not $K_i$ and $k_3$) are related to participant sex, weight and insulin levels, which is consistent with our findings for SUVR[13]. This seems to suggest that individual differences in peripheral metabolism may alter how glucose is delivered to supply the brain's functional needs[67], thereby affecting individual $K_1$-BOLD coupling. This is an interesting area of investigation into the crosstalk between brain and periphery, which could help to reveal how and why metabolic diseases, such as diabetes, lead to increased risk of developing neurological disorders (e.g., Alzheimer's disease[68]).

Some limitations need to be considered. First, PET and rs-fMRI data were not acquired simultaneously. While this may introduce some within-individual variability[69], we have shown a better match between SUVR and rs-fMRI using sequentially acquired data in our previous work[13]. This may relate to the high quality of the rs-fMRI data employed in this study (HCP

Aging[70]). Second, PET kinetic estimates in this study are not truly fully quantitative. For [$^{18}$F]FDG, using an image-derived input function, which is likely to still be affected by PVEs due to the limited spatial resolution of the HR+ scanner (FWHM ~5 mm)[71], may make $K_i$, $K_1$ and $k_3$ estimates biased. However, their *relative* spatial distribution across ROIs, which was the focus of our analyses, is expected to not be impacted. The same reasoning applies to [$^{15}$O]$H_2O$ and [$^{15}$O]$O_2$ data. Third, the low spatial resolution of the HR+ scanner and relatively high noise level in the data makes nonlinear fitting of complex compartment model structures problematic. However, the variational Bayesian framework[31] we used allowed us to retrieve accurate and precise estimates at the voxel level even in such contexts. We thus believe our [$^{18}$F]FDG kinetic parameter maps are faithful representations of their spatial distribution. Re-assessing these results on high-sensitivity, high-resolution PET scanners[72,73,74] will be important to confirm the reproducibility of these spatial patterns, possibly capture more details, and further validate their biological meaning. Fourth, it must also be remembered that the BOLD signal is only an indirect measure of neuronal activity, which is subjected to significant contamination from systemic modulations (heart rate variability, vasomotion, respiratory volume variability etc.)[75]. Lastly, despite the use of sophisticated modeling, this work remains correlational: only a controlled perturbational approach may fully elucidate causal links between glucose metabolism and spontaneous activity.

In conclusion, we have comprehensively assessed the physiological information contained in [$^{18}$F]FDG dynamic PET data from a large dataset of 47 healthy individuals, estimating both the macroparameter $K_i$ (uptake), and the rate constants $K_1$ (delivery) and $k_3$ (phosphorylation), with unprecedented spatial detail, to demonstrate how the microparameters add relevant information. We then used the combination of rs-fMRI measures previously identified as the best suited to

explain SUVR variance across regions, and verified that they explain a similar portion of $K_i$ variability (less so for $K_1$ and $k_3$). Metrics based on BOLD local properties (*ReHo*) are again most tightly related to glucose metabolism ($K_i$ and $k_3$). The inclusion of CBF and $CMRO_2$ markedly improves the description of $K_i$; moreover, $K_1$ was coupled with $CMRO_2$ more than any other feature. Overall, this work enriches the landscape of our understanding of the interplay between PET- and BOLD-derived variables, which reflect complex interactions between brain metabolism (CMRglc, $CMRO_2$), blood flow and neural activity. With high-performance PET scanners, assessment of glucose delivery ($K_1$) and hexokinase activity ($k_3$) via [$^{18}$F]FDG PET may become useful for evaluating disorders of the brain (e.g., Alzheimer's disease[19]; traumatic brain injury[21]) and other organs[76].

**Funding**

Funding for the acquisitions and managing of the Adult Metabolism & Brain Resilience dataset in Washington University in Saint Louis was provided by NIH/NIA R01AG053503, R01AG057536, and RF1AG073210. Some of the MRI sequences used were obtained from the Massachusetts General Hospital.

**Authors' contributions**

TV and AB designed the research. TV analyzed the data. TV, JJL, AGV, MSG, MC and AB interpreted the results. TV wrote the manuscript. TV, JJL, AGV, MSG, MC and AB revised the manuscript.

**Declaration of conflicting interests**

The authors declared no potential conflicts of interest with respect to the research, authorship, and/or publication of this article.

**ORCID:**

Volpi https://orcid.org/0000-0002-5451-6710

Lee https://orcid.org/0000-0003-2269-6267

Vlassenko https://orcid.org/0000-0002-4776-4855

Goyal https://orcid.org/0000-0003-1970-4270

Corbetta https://orcid.org/0000-0001-8295-3304

Bertoldo https://orcid.org/0000-0002-6262-6354

## References

1. Roy CS, Sherrington CS. On the Regulation of the Blood-supply of the Brain. *The Journal of Physiology*. 1890 Jan 1;11(1–2):85–158.
2. Raichle ME. Behind the scenes of functional brain imaging: A historical and physiological perspective. *Proc Natl Acad Sci*. 1998 Feb 3;95(3):765–72.
3. Sokoloff L, Mangold R, Wechsler RL, Kennedy C, Kety SS. The effect of mental arithmetic on cerebral circulation and metabolism. *J Clin Invest*. 1955;34(7):1101–8.
4. Raichle ME. The Brain's Dark Energy. *Science*. 2006;314(5803):1249–50.
5. Clarke DD, Sokoloff L. Circulation and energy metabolism in the brain. In: Siegel GJ, Agranoff BW, Albers RW, et al., (eds.), Basic neurochemistry: molecular, cellular and medical aspects. 6th edn, Ch. 31. Philadelphia: Lippincott-Raven, 1999.
6. Fox MD, Raichle ME. Spontaneous fluctuations in brain activity observed with functional magnetic resonance imaging. *Nat Rev Neurosci*. 2007 Sep;8(9):700–11.
7. Raichle ME. Correlation Between Regional Cerebral Blood Flow and Oxidative Metabolism: In Vivo Studies in Man. *Arch Neurol*. 1976 Aug 1;33(8):523.
8. Deng S, Franklin CG, O'Boyle M, Zhang W, Heyl BL, Jerabek PA, et al. Hemodynamic and metabolic correspondence of resting-state voxel-based physiological metrics in healthy adults. *NeuroImage*. 2022 Apr;250:118923.
9. Tomasi D, Wang GJ, Volkow ND. Energetic cost of brain functional connectivity. *Proc Natl Acad Sci USA*. 2013 Aug;110(33):13642–7.
10. Riedl V, Bienkowska K, Strobel C, Tahmasian M, Grimmer T, Forster S, et al. Local Activity Determines Functional Connectivity in the Resting Human Brain: A Simultaneous FDG PET/fMRI Study. *J Neurosci*. 2014 Apr 30;34(18):6260–6.

11. Aiello M, Salvatore E, Cachia A, Pappatà S, Cavaliere C, Prinster A, et al. Relationship between simultaneously acquired resting-state regional cerebral glucose metabolism and functional MRI: A PET/MR hybrid scanner study. *NeuroImage*. 2015;113:111–21.
12. Palombit A, Silvestri E, Volpi T, Aiello M, Cecchin D, Bertoldo A, et al. Variability of regional glucose metabolism and the topology of functional networks in the human brain. *NeuroImage*. 2022 May;119280.
13. Volpi T, Silvestri E, Aiello M, Lee JJ, Vlassenko AG, Goyal MS, et al. The brain's "dark energy" puzzle: How strongly is glucose metabolism linked to resting-state brain activity? *J Cereb Blood Flow Metab*. 2024 Mar 5;0271678X241237974.
14. Barrio JR, Huang SC, Satyamurthy N, Scafoglio CS, Yu AS, Alavi A, et al. Does 2-FDG PET Accurately Reflect Quantitative In Vivo Glucose Utilization? *J Nucl Med*. 2020 Jun;61(6):931–7.
15. Sokoloff L, Reivich M, Kennedy C, Rosiers MHD, Patlak CS, Pettigrew KD, et al. The [14C]deoxyglucose method for the measurement of local cerebral glucose utilization: theory, procedure, and normal values in the conscious and anesthetized albino rat. *J Neurochem*. 1977; 28(5): 897–916.
16. Bertoldo A, Rizzo G, Veronese M. Deriving physiological information from PET images: From SUV to compartmental modelling. *Clin Transl Imaging*. 2014;2(3):239–51.
17. Crone C. The Permeability of Capillaries in Various Organs as Determined by Use of the 'Indicator Diffusion' Method. *Acta Physiol Scandin*. 1963 Aug;58(4):292–305.
18. Furler SM, Jenkins AB, Storlien LH, Kraegen EW. In vivo location of the rate-limiting step of hexose uptake in muscle and brain tissue of rats. *Am J Physiol Endocrinol Metab*. 1991 Sep 1;261(3):E337–47.
19. Piert M, Koeppe RA, Giordani B, Berent S, Kuhl DE. Diminished glucose transport and phosphorylation in Alzheimer's disease determined by dynamic FDG-PET. *J Nucl Med*. 1996 Feb;37(2):201–8.

20. Heiss WD, Pawlik G, Herholz K, Wagner R, Göldner H, Wienhard K. Regional Kinetic Constants and Cerebral Metabolic Rate for Glucose in Normal Human Volunteers Determined by Dynamic Positron Emission Tomography of [ 18 F]-2-Fluoro-2-Deoxy-D-Glucose. *J Cereb Blood Flow Metab*. 1984 Jun;4(2):212–23.
21. Hermanides J, Hong YT, Trivedi M, Outtrim J, Aigbirhio F, Nestor PJ, et al. Metabolic derangements are associated with impaired glucose delivery following traumatic brain injury. *Brain*. 2021 Dec 16;144(11):3492–504.
22. Wu GR, Liao W, Stramaglia S, Ding JR, Chen H, Marinazzo D. A blind deconvolution approach to recover effective connectivity brain networks from resting state fMRI data. *Med Image Anal*. 2013 Apr;17(3):365–74.
23. Yeo BTT, Krienen FM, Sepulcre J, Sabuncu MR, Lashkari D, Hollinshead M, et al. The organization of the human cerebral cortex estimated by intrinsic functional connectivity. *J Neurophys*. 2011;106(3):1125–65.
24. Allen EA, Damaraju E, Plis SM, Erhardt EB, Eichele T, Calhoun VD. Tracking whole-brain connectivity dynamics in the resting state. *Cereb Cortex*. 2014 Mar;24(3):663–76.
25. Vaishnavi SN, Vlassenko AG, Rundle MM, Snyder AZ, Mintun MA, Raichle ME. Regional aerobic glycolysis in the human brain. *Proc Natl Acad Sci USA*. 2010 Oct 12;107(41):17757–62.
26. Goyal MS, Blazey T, Metcalf NV, McAvoy MP, Strain JF, Rahmani M, et al. Brain aerobic glycolysis and resilience in Alzheimer disease. *Proc Natl Acad Sci USA*. 2023 Feb 14;120(7):e2212256120.
27. Jenkinson M, Bannister P, Brady M, Smith S. Improved Optimization for the Robust and Accurate Linear Registration and Motion Correction of Brain Images. *NeuroImage*. 2002; 17(2): 825–841.
28. Silvestri, E., Volpi, T., Bettinelli, A., De Francisci, M., Jones, J., Corbetta, M., et al. Image-derived Input Function in brain [18F]FDG PET studies: which alternatives to the carotid

syphons? In: 2022 44th Annual International Conference of the IEEE Engineering in Medicine & Biology Society (EMBC). 2022; 243-6.

29. Peruzzo D, Bertoldo A, Zanderigo F, Cobelli C. Automatic selection of arterial input function on dynamic contrast-enhanced MR images. Computer Methods and Programs in Biomedicine. 2011; 104(3): e148–157.
30. Chen K, Bandy D, Reiman E, Huang S-C, Lawson M, Feng D, et al. Noninvasive Quantification of the Cerebral Metabolic Rate for Glucose Using Positron Emission Tomography, 18 F-Fluoro-2-Deoxyglucose, the Patlak Method, and an Image-Derived Input Function. J Cereb Blood Flow Metab. 1998; 18(7): 716–723.
31. Castellaro M, Rizzo G, Tonietto M, Veronese M, Turkheimer FE, Chappell MA, et al. A Variational Bayesian inference method for parametric imaging of PET data. *NeuroImage*. 2017;150(Oct. 2016):136–49.
32. Volpi T, Vallini G, Silvestri E, De Francisci M, Durbin T, Corbetta M, et al. A new framework for metabolic connectivity mapping using bolus [18F]FDG PET and kinetic modeling. *J Cereb Blood Flow Metab*. 2023 Jun 28;0271678X231184365.
33. Kety SS, Schmidt CF. The Determination Of Cerebral Blood Flow In Man By The Use Of Nitrous Oxide In Low Concentrations. Am J Physiol. 1945 Jan 1;143(1):53–66.
34. Ssali T, Anazodo UC, Thiessen JD, Prato FS, St. Lawrence K. A Noninvasive Method for Quantifying Cerebral Blood Flow by Hybrid PET/MRI. J Nucl Med. 2018 Aug;59(8):1329–34.
35. Narciso L, Ssali T, Iida H, St Lawrence K. A non-invasive reference-based method for imaging the cerebral metabolic rate of oxygen by PET/MR: theory and error analysis. Phys Med Biol. 2021 Mar 21;66(6):065009.
36. Schaefer A, Kong R, Gordon EM, Laumann TO, Zuo XN, Holmes AJ, et al. Local-Global Parcellation of the Human Cerebral Cortex from Intrinsic Functional Connectivity MRI. *Cereb Cortex*. 2018 Sep 1;28(9):3095–114.

37. Hammers A, Allom R, Koepp MJ, Free SL, Myers R, Lemieux L, et al. Three-dimensional maximum probability atlas of the human brain, with particular reference to the temporal lobe. *Hum Brain Mapp*. 2003; 19(4): 224–247.

38. Rousset O, Rahmim A, Alavi A, Zaidi H. Partial Volume Correction Strategies in PET. *PET Clin*. 2007 Apr;2(2):235–49.

39. Henriksen OM, Vestergaard MB, Lindberg U, Aachmann-Andersen NJ, Lisbjerg K, Christensen SJ, et al. Interindividual and regional relationship between cerebral blood flow and glucose metabolism in the resting brain. *J Appl Physiol* (1985). 2018 Oct 1;125(4):1080–9.

40. Greve DN, Salat DH, Bowen SL, Izquierdo-Garcia D, Schultz AP, Catana C, et al. Different partial volume correction methods lead to different conclusions: An 18F-FDG-PET study of aging. *NeuroImage*. 2016 May;132:334–43.

41. Behzadi Y, Restom K, Liau J, Liu TT. A component-based noise correction method (CompCor) for BOLD and perfusion based fMRI. *NeuroImage*. 2007;37(1):90–101.

42. Ciric R, Wolf DH, Power JD, Roalf DR, Baum GL, Ruparel K, et al. Benchmarking of participant-level confound regression strategies for the control of motion artifact in studies of functional connectivity. *NeuroImage*. 2017;154:174–87.

43. Power JD, Mitra A, Laumann TO, Snyder AZ, Schlaggar BL, Petersen SE. Methods to detect, characterize, and remove motion artifact in resting state fMRI. *NeuroImage*. 2014;84:320–41.

44. Sokunbi MO, Staff RT, Waiter GD, Ahearn TS, Fox HC, Deary IJ, et al. Inter-individual Differences in fMRI Entropy Measurements in Old Age. *IEEE Trans Biomed Eng*. 2011 Nov;58(11):3206–14.

45. Zou QH, Zhu CZ, Yang Y, Zuo XN, Long XY, Cao QJ, et al. An improved approach to detection of amplitude of low-frequency fluctuation (ALFF) for resting-state fMRI: Fractional ALFF. *J Neurosci Meth*. 2008 Jul;172(1):137–41.

46. Zang Y, Jiang T, Lu Y, He Y, Tian L. Regional homogeneity approach to fMRI data analysis. *NeuroImage*. 2004;22(1):394–400.

47. Buxton RB, Frank LR. A Model for the Coupling between Cerebral Blood Flow and Oxygen Metabolism during Neural Stimulation. *J Cereb Blood Flow Metab*. 1997 Jan;17(1):64–72.
48. Wu GR, Marinazzo D. Sensitivity of the resting-state haemodynamic response function estimation to autonomic nervous system fluctuations. *Phil Trans R Soc A*. 2016 May 13;374(2067):20150190.
49. Rubinov M, Sporns O. Complex network measures of brain connectivity: uses and interpretations. *NeuroImage*. 2010;52(3):1059–69.
50. Cabral J, Vidaurre D, Marques P, Magalhães R, Silva Moreira P, Miguel Soares J, et al. Cognitive performance in healthy older adults relates to spontaneous switching between states of functional connectivity during rest. *Sci Rep*. 2017;7(1).
51. Shapiro SS, Wilk MB. An analysis of variance test for normality (complete samples). *Biometrika*. 1965 Dec 1;52(3–4):591–611.
52. Steiger JH. Tests for comparing elements of a correlation matrix. *Psychol Bull*. 1980; *87*(2), 245–251.
53. Mu□ller S, Scealy JL, Welsh AH. Model Selection in Linear Mixed Models. *Statist Sci*. 2013 May 1; 28(2).
54. Belsley DA. Conditioning diagnostics: collinearity and weak data in regression. New York: Wiley; 1991. 396 p. (Probability and mathematical statistics).
55. Cobelli C, DiStefano JJ. Parameter and structural identifiability concepts and ambiguities: a critical review and analysis. *Am J Physiol Regul Integr Comp Physiol*. 1980 Jul 1;239(1):R7–24.
56. Hox JJ, Moerbeek M, Schoot R van de. Multilevel analysis: techniques and applications. Third edition. New York, NY: Routledge; 2017. (Quantitative methodology series).
57. Magistretti PJ, Allaman I. A Cellular Perspective on Brain Energy Metabolism and Functional Imaging. *Neuron*. 2015 May;86(4):883–901.
58. Attwell D, Laughlin SB. An Energy Budget for Signaling in the Grey Matter of the Brain. *J Cereb Blood Flow Metab*. 2001.

59. Hamberg LM, Hunter GJ, Alpert NM, Choi NC, Babich JW, Fischman AJ. The dose uptake ratio as an index of glucose metabolism: useful parameter or oversimplification? *J Nucl Med*. 1994 Aug;35(8):1308–12.

60. Huang SC. Anatomy of SUV. *Nucl Med Biol*. 2000 Oct;27(7):643–6.

61. Koeppe RA, Frey KA, Snyder SE, Meyer P, Kilbourn MR, Kuhl DE. Kinetic Modeling of N -[11C]Methylpiperidin-4-yl Propionate: Alternatives for Analysis of an Irreversible Positron Emission Tomography Tracer for Measurement of Acetylcholinesterase Activity in Human Brain. *J Cereb Blood Flow Metab*. 1999 Oct;19(10):1150–63.

62. Glasser MF, Goyal MS, Preuss TM, Raichle ME, Van Essen DC. Trends and properties of human cerebral cortex: Correlations with cortical myelin content. *NeuroImage*. 2014 Jun;93:165–75.

63. Cho J, Lee J, An H, Goyal MS, Su Y, Wang Y. Cerebral oxygen extraction fraction (OEF): Comparison of challenge-free gradient echo QSM+qBOLD (QQ) with $^{15}$O PET in healthy adults. *J Cereb Blood Flow Metab*. 2021 Jul;41(7):1658–68.

64. Ito H, Ibaraki M, Yamakuni R, Hakozaki M, Ukon N, Ishii S, et al. Oxygen extraction fraction is not uniform in human brain: a positron emission tomography study. *J Physiol Sci*. 2023 Oct 12;73(1):25.

65. Herculano-Houzel S. The glia/neuron ratio: How it varies uniformly across brain structures and species and what that means for brain physiology and evolution: The Glia/Neuron Ratio. *Glia*. 2014 Sep;62(9):1377–91.

66. Huisman MC, van Golen LW, Hoetjes NJ, Greuter HN, Schober P, Ijzerman RG, et al. Cerebral blood flow and glucose metabolism in healthy volunteers measured using a high resolution PET scanner. *EJNMMI Res*. 2012;2(1):63.

67. Rebelos E, Bucci M, Karjalainen T, Oikonen V, Bertoldo A, Hannukainen JC, et al. Insulin Resistance Is Associated With Enhanced Brain Glucose Uptake During Euglycemic Hyperinsulinemia: A Large-Scale PET Cohort. *Diabetes Care*. 2021 Mar 1;44(3):788–94.

68. Biessels GJ, Despa F. Cognitive decline and dementia in diabetes mellitus: mechanisms and clinical implications. *Nat Rev Endocrinol*. 2018 Oct;14(10):591–604.

69. Cecchin D, Palombit A, Castellaro M, Silvestri E, Bui F, Barthel H, et al. Brain PET and functional MRI: Why simultaneously using hybrid PET/MR systems? *Q J Nucl Med Mol Imaging*. 2017;61(4):345–59.

70. Elam JS, Glasser MF, Harms MP, Sotiropoulos SN, Andersson JLR, Burgess GC, et al. The Human Connectome Project: A retrospective. *NeuroImage*. 2021 Dec;244:118543.

71. Volpi T, Maccioni L, Colpo M, Debiasi G, Capotosti A, Ciceri T, et al. An update on the use of image-derived input functions for human PET studies: new hopes or old illusions? *EJNMMI Res*. 2023 Nov 10;13(1):97.

72. Meikle SR, Sossi V, Roncali E, Cherry SR, Banati R, Mankoff D, et al. Quantitative PET in the 2020s: a roadmap. *Phys Med Biol*. 2021 Mar 21;66(6):06RM01.

73. Li H, Badawi RD, Cherry SR, Fontaine K, He L, Henry S, et al. Performance Characteristics of the NeuroEXPLORER, a Next-Generation Human Brain PET/CT Imager. *J Nucl Med*. 2024 Aug;65(8):1320–6.

74. Lee JJ, Metcalf N, Durbin TA, Byers J, Casey K, Jafri H, et al. Multi-Tracer Studies of Brain Oxygen and Glucose Metabolism Using a Time-of-Flight Positron Emission Tomography - Computed Tomography Scanner. *JoVE*. 2024 Jun 7;(208):65510.

75. Chen JE, Lewis LD, Chang C, Tian Q, Fultz NE, Ohringer NA, et al. Resting-state “physiological networks.” *NeuroImage*. 2020;213.

76. Wang Y, Spencer BA, Schmall J, Li E, Badawi RD, Jones T, et al. High-Temporal-Resolution Lung Kinetic Modeling Using Total-Body Dynamic PET with Time-Delay and Dispersion Corrections. *J Nucl Med*. 2023 Apr 28;jnumed.122.264810.

77. Garrett DD, Kovacevic N, McIntosh AR, Grady CL. Blood Oxygen Level-Dependent Signal Variability Is More than Just Noise. *J Neurosci*. 2010 Apr 7;30(14):4914–21.

78. Amor TA, Russo R, Diez I, Bharath P, Zirovich M, Stramaglia S, et al. Extreme brain events: Higher-order statistics of brain resting activity and its relation with structural connectivity. *EPL*. 2015;111(6).

79. Omidvarnia A, Mesbah M, Pedersen M, Jackson G. Range Entropy: A Bridge between Signal Complexity and Self-Similarity. *Entropy*. 2018 Dec 13;20(12):962.

80. Deng L, Sun J, Cheng L, Tong S. Characterizing dynamic local functional connectivity in the human brain. *Sci Rep*. 2016 May;6.

81. Hellyer PJ, Barry EF, Pellizzon A, Veronese M, Rizzo G, Tonietto M, et al. Protein synthesis is associated with high-speed dynamics and broad-band stability of functional hubs in the brain. *NeuroImage*. 2017 Jul;155:209–16.

82. Pedersen M, Omidvarnia A, Walz JM, Zalesky A, Jackson GD. Spontaneous brain network activity: Analysis of its temporal complexity. *Net Neurosci*. 2017 Jun;1(2):100–15.

# Figures

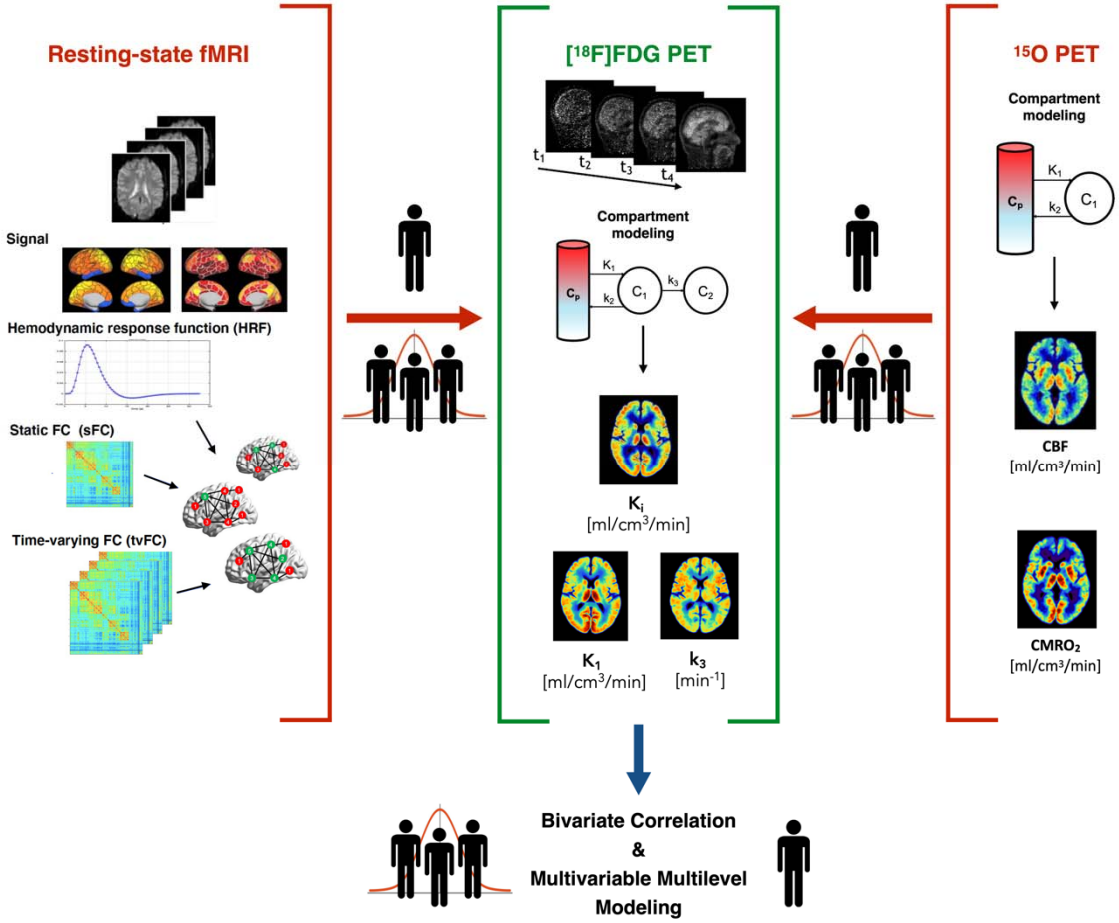


**Figure 1**: Flowchart of the analysis. The rs-fMRI data (*left*) were used to extract fifty features representative of four "pools", i.e., 1) *signal* and *local* measures, 2) hemodynamic response function (*HRF*), 3) static functional connectivity (*sFC*), 4) time-varying functional connectivity (*tvFC*), which were parceled into 216 ROIs. [$^{18}$F]FDG dynamic PET data (*center*) were fitted with an irreversible two-tissue compartment model to obtain voxel-wise estimates of [$^{18}$F]FDG kinetic parameters (most importantly, for the purpose of the analyses, $K_i$, $K_1$ and $k_3$), which were also parceled. [$^{15}$O]$H_2O$ and [$^{15}$O]$O_2$ dynamic PET data (*top right*) were also quantified using a reversible one-tissue compartment model to obtain estimates of CBF and $CMRO_2$, which were also parceled. The spatial coupling across ROIs between *predictors* (A) rs-fMRI features, B) CBF and $CMRO_2$) – marked in *red*, and *outcomes* ([$^{18}$F]FDG kinetic parameters $K_i$, $K_1$ and $k_3$) – marked in *green*, was investigated on two levels, i.e., at group-average

level (*three-persons icon*) and at individual level (*one-person icon*) via bivariate correlation and multivariable multilevel modeling.

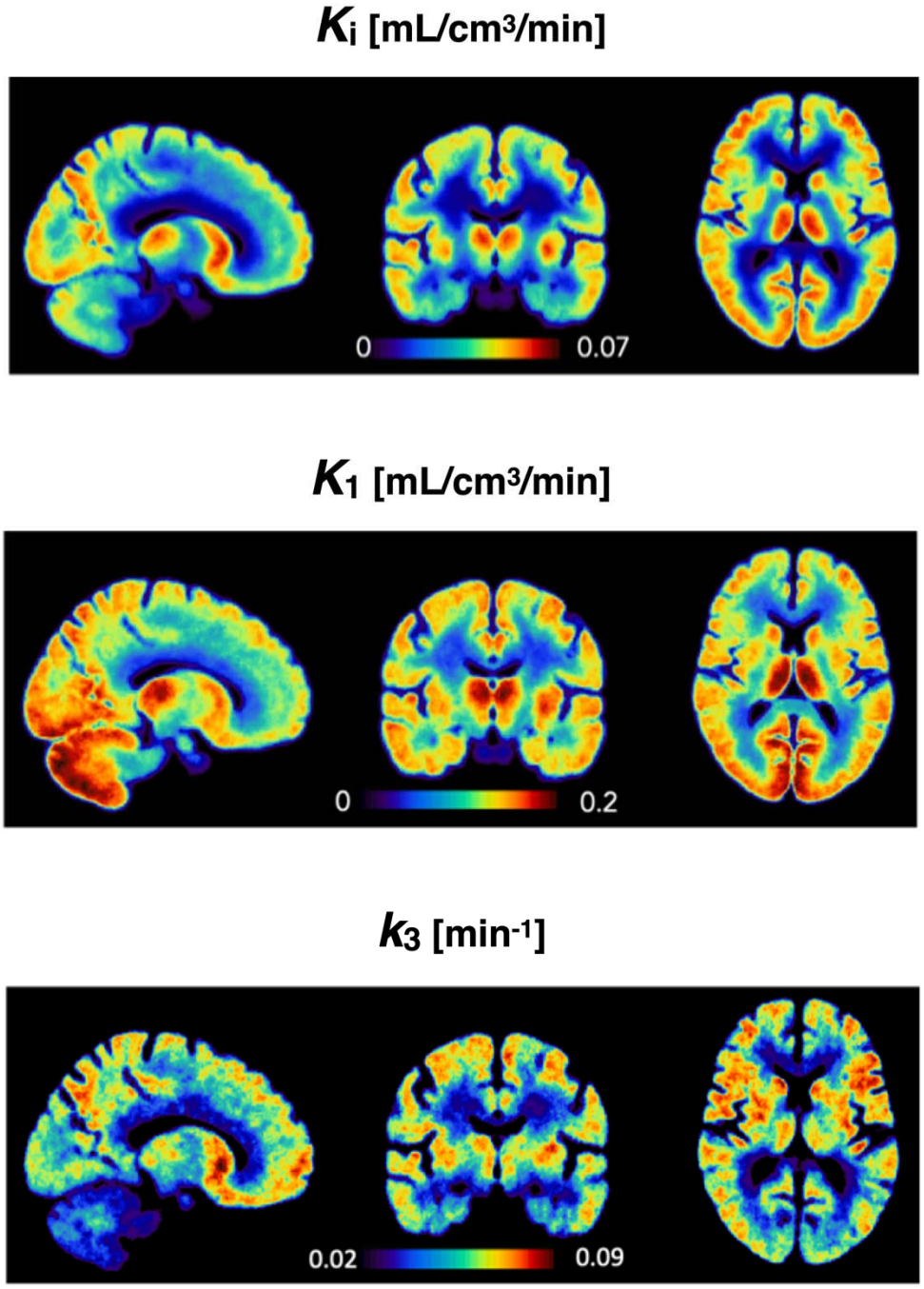


**Figure 2**: Group-average [$^{18}$F]FDG PET parametric maps (n = 47) for $K_i$, $K_1$, $k_3$ in MNI space, generated using the Variational Bayesian inference algorithm[31].

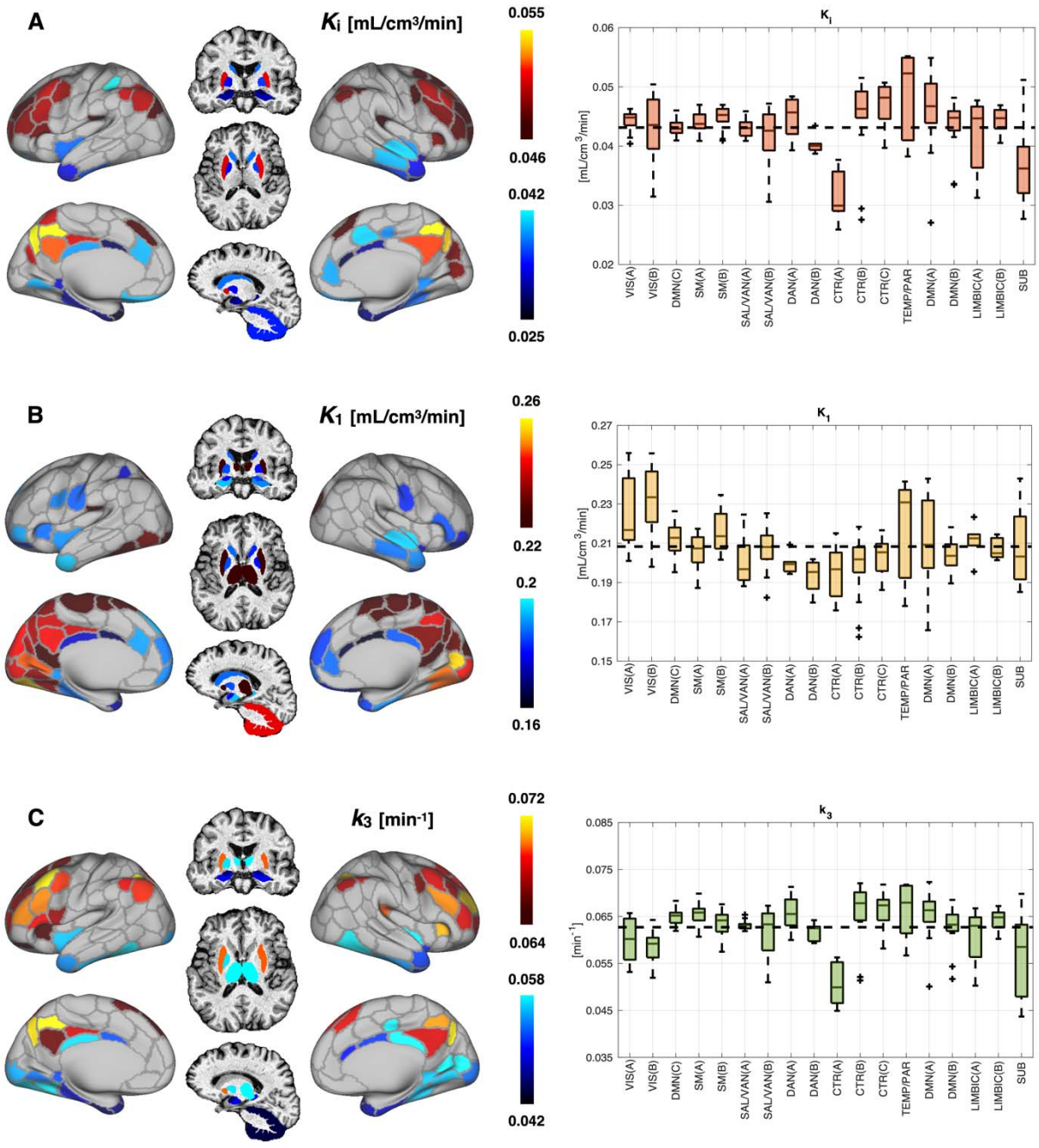


**Figure 3**: Top and bottom 20% values of group-average $K_i$ (**A**), $K_1$ (**B**) and $k_3$ (**C**), along with corresponding boxplots showing group-average regional values of each parameter divided according to Schaefer's functional brain networks.

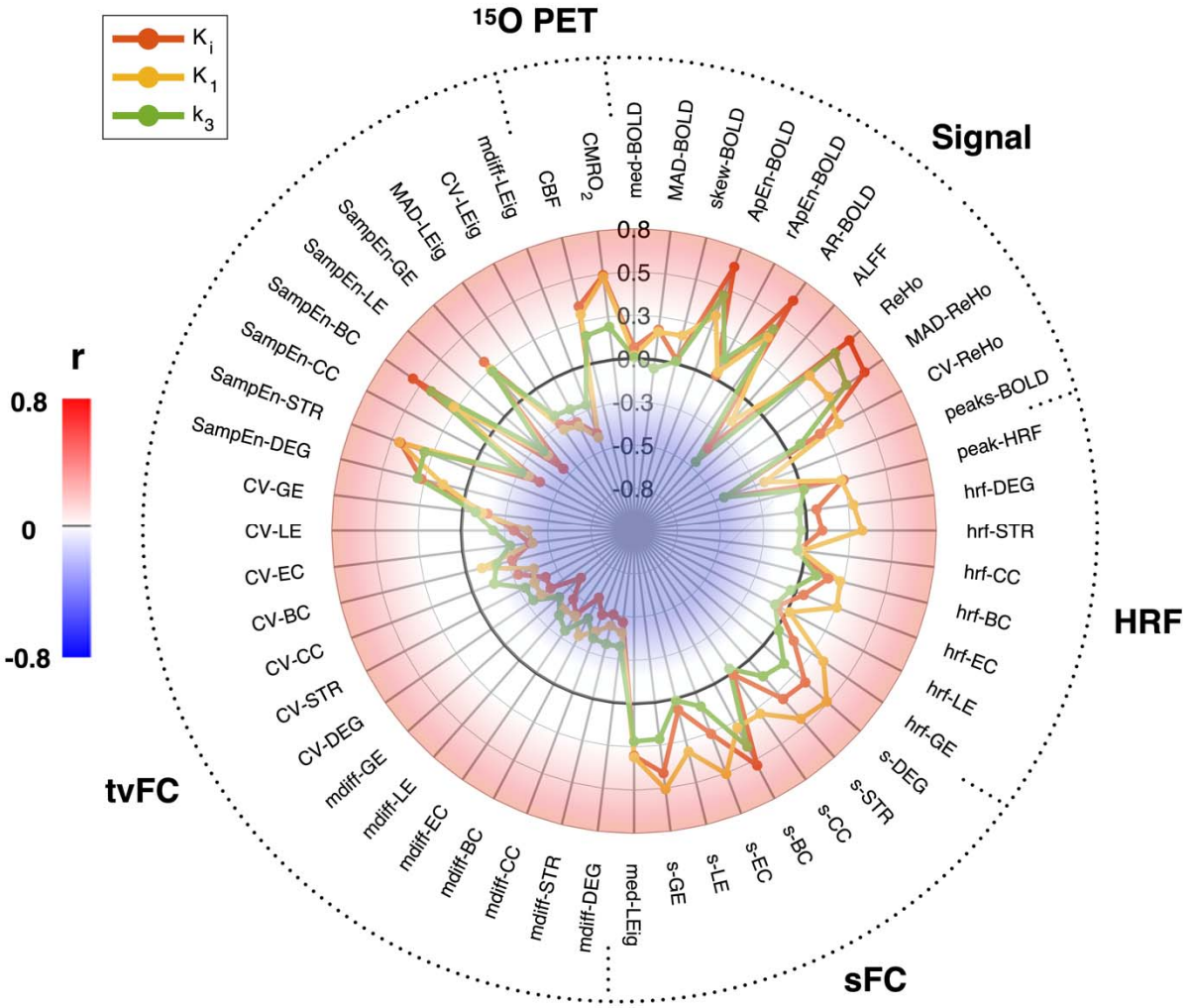


**Figure 4**: Spider plot of Pearson's correlations across brain regions between group-average [$^{18}$F]FDG kinetic parameters ($K_i$, $K_1$ and $k_3$) vs. group-average rs-fMRI features (divided into 4 a priori defined pools: 1) signal, 2) HRF, 3) sFC, 4) tvFC), and CBF and CMRO$_2$ ($^{15}$O PET).

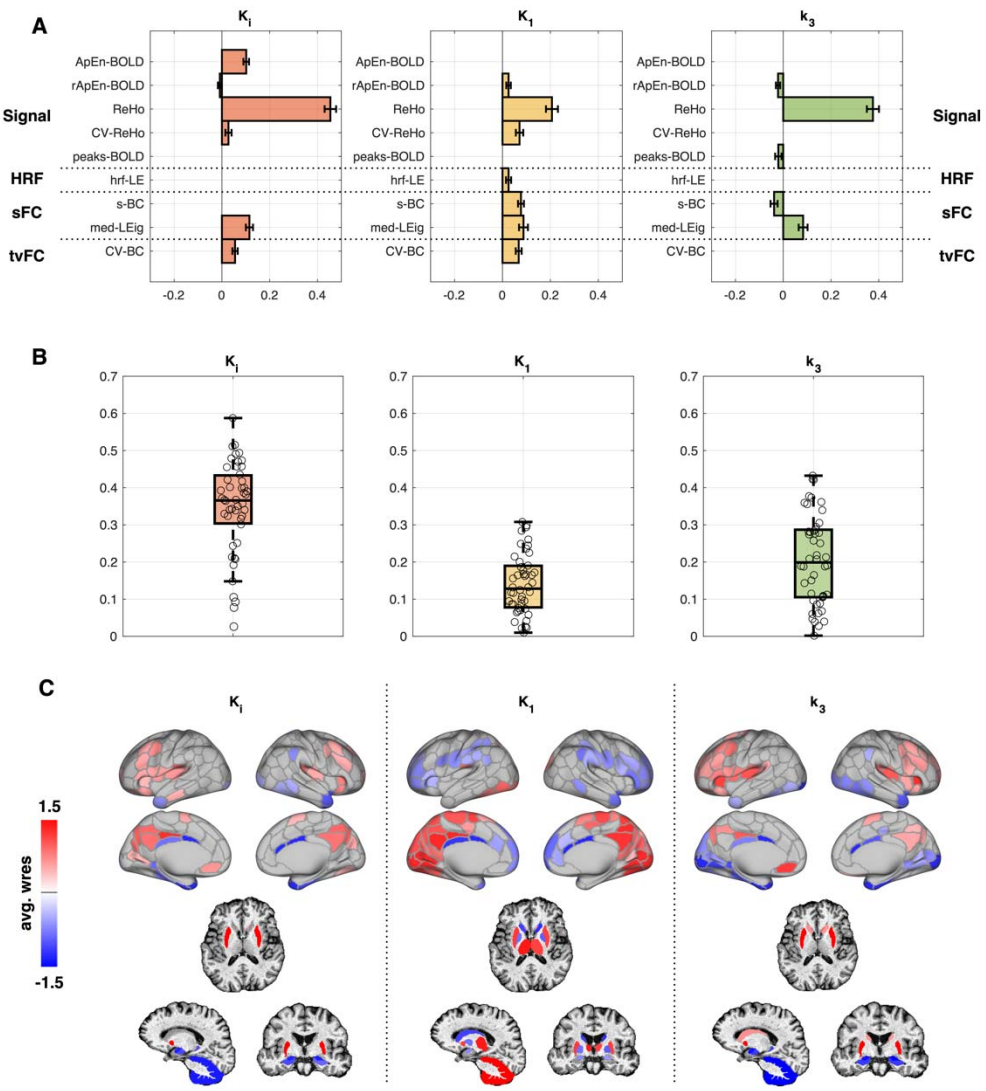


**Figure 5.** Multilevel modeling of glucose metabolism: *rs-fMRI-only models*. Fixed effects (adapted 9-parameter model) for [$^{18}$F]FDG kinetic parameters ($K_i$, $K_1$ and $k_3$): estimate weights and standard errors (SEs), which represent the parameters that best explain $K_i$, $K_1$ and $k_3$ across brain regions at group level (**A**). The empty spaces correspond to features whose estimates have unacceptable precision (%SE > 100%) at group level, or estimates not significantly different from zero. Boxplots of individual $R^2$ values $R^2_i$ (median and boxes of 25$^{th}$ and 75$^{th}$ percentile in overlay) representing the spatial variance of $K_i$, $K_1$ and $k_3$ explained by the BOLD-based predictors at individual level (**B**). Across-individual average of weighted residuals of the multilevel model (*avg. wres*), visualized in the [[-1.5,-0.5];[0.5,1.5]] range for each brain region (**C**).

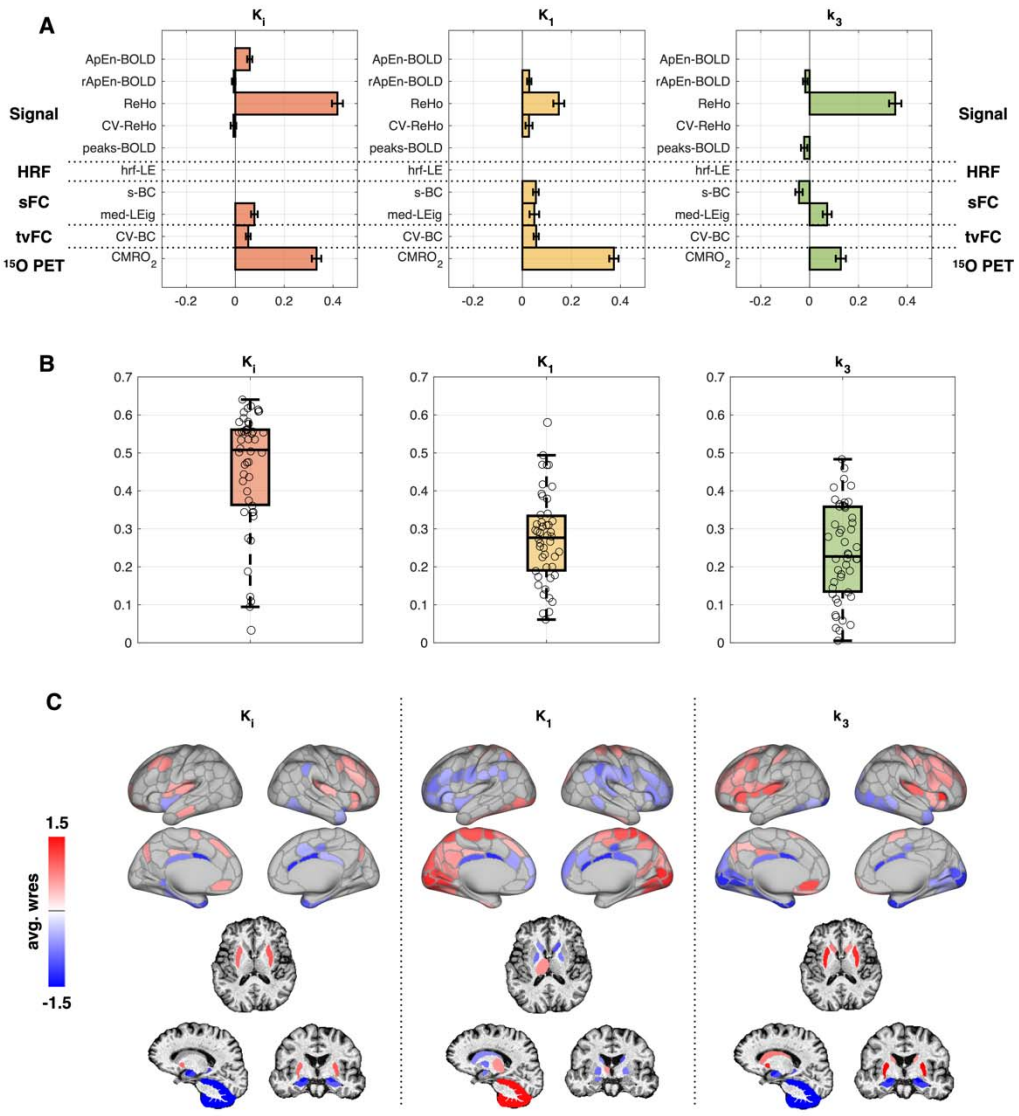


**Figure 6.** Multilevel modeling of glucose metabolism: *rs-fMRI plus $CMRO_2$ models*. Fixed effects (adapted 9-parameter model + $CMRO_2$) for [$^{18}$F]FDG kinetic parameters ($K_i$, $K_1$ and $k_3$): estimate weights and standard errors (SEs), which represent the parameters that best explain $K_i$, $K_1$ and $k_3$ across brain regions at group level (**A**). The empty spaces correspond to features whose estimates have unacceptable precision (%SE > 100%) at group level, or estimates not significantly different from zero. Boxplot of individual $R^2$ values $R^2_i$ (median and boxes of 25$^{th}$ and 75$^{th}$ percentile in overlay) representing the spatial variance of $K_i$, $K_1$ and $k_3$ explained by the predictors at individual level (**B**). Across-individual average of weighted residuals of the multilevel model (*avg. wres*), visualized in the [[-1.5,-0.5];[0.5,1.5]] range for each brain region (**C**).

# Tables

## Table 1. Extracted rs-fMRI features and their categories.

Fifty fMRI-derived variables, divided according to the pool to which they belong: 1) signal, 2) hemodynamic response function (HRF), 3) static functional connectivity (sFC), 4) time-varying functional connectivity (tvFC). See **Supplementary Methods** for full description of the features.

| ***Pools*** | ***rs-fMRI Variables*** |
|---|---|
| **Signal** | **med-BOLD**: median of the BOLD time series[45] |
| | **MAD-BOLD**: median absolute deviation (MAD) of the BOLD time series[77] |
| | **skew-BOLD**: skewness of the BOLD time series[78] |
| | **ApEn-BOLD**: approximate entropy (ApEn) of the BOLD time series[44] |
| | **rApEn-BOLD**: range ApEn of the BOLD time series[79] |
| | **AR-BOLD**: reflection coefficient of the first-order autoregressive AR(1) model fit to BOLD time series[79] |
| | **ALFF**: amplitude of low frequency fluctuations (ALFF) of BOLD time series[45] |
| | **ReHo**: regional homogeneity of BOLD time series[46] |
| | **MAD-ReHo**: MAD of the time-varying ReHo (tvReHo)[80] |
| | **CV-ReHo**: percent coefficient of variation of tvReHo[80] |
| | **peaks-BOLD**: number of BOLD pseudo-events[22] |
| **HRF** | **peak-HRF**: height of HRF peak[22] |
| | **hrf-DEG**: degree (DEG) of HRF correlation matrix [*original metric*] |
| | **hrf-STR**: strength (STR) of HRF correlation matrix [*original metric*] |
| | **hrf-CC**: clustering coefficient (CC) of HRF correlation matrix [*original metric*] |
| | **hrf-BC**: betweenness centrality (BC) of HRF correlation matrix [*original metric*] |
| | **hrf-EC**: eigenvector centrality (EC) of HRF correlation matrix [*original metric*] |
| | **hrf-LE**: local efficiency (LE) of HRF correlation matrix [*original metric*] |
| | **hrf-GE**: global efficiency (GE) of HRF correlation matrix [*original metric*] |
| **sFC** | **s-DEG**: DEG of sFC[49] |
| | **s-STR**: STR of sFC[49] |
| | **s-CC**: CC of sFC[49] |
| | **s-BC**: BC of sFC[49] |
| | **s-EC**: EC of sFC[49] |
| | **s-LE**: LE of sFC[49] |
| | **s-GE**: GE of sFC[49] |
| | **med-LEig**: median of the Leading Eigenvector (LEig)'s time series[50] |
| **tvFC** | **mdiff-DEG**: temporal median of the differentials (mdiff) of DEG time series [*original metric*] |
| | **mdiff-STR**: mdiff of STR time series [*original metric*] |
| | **mdiff-CC**: mdiff of CC time series [*original metric*] |
| | **mdiff-BC**: diff of BC time series [*original metric*] |
| | **mdiff-EC**: mdiff of EC time series [*original metric*] |
| | **mdiff-LE**: mdiff of LE time series [*original metric*] |

| | |
|---|---|
| | **mdiff-GE**: mdiff of GE time series [*original metric*] |
| | **CV-DEG**: coefficient of variation of DEG time series[81] |
| | **CV-STR**: percent coefficient of variation of STR time series[81] |
| | **CV-CC**: percent coefficient of variation of CC time series[81] |
| | **CV-BC**: percent coefficient of variation of BC time series[81] |
| | **CV-EC**: percent coefficient of variation of EC time series[81] |
| | **CV-LE**: percent coefficient of variation of LE time series[81] |
| | **CV-GE:** percent coefficient of variation of GE time series[81] |
| | **SampEn-DEG**: sample entropy (SampEn) of DEG time series[82] |
| | **SampEn-STR**: SampEn of STR time series[82] |
| | **SampEn-CC**: SampEn of CC time series[82] |
| | **SampEn-BC**: SampEn of BC time series[82] |
| | **SampEn-LE**: SampEn of LE time series[82] |
| | **SampEn-GE**: SampEn of GE time series[82] |
| | **MAD-LEig**: MAD of LEig time series[50] |
| | **CV-LEig**: percent coefficient of variation of LEig time series[50] |
| | **mdiff-LEig**: mdiff of LEig time series[50] |

## Resting-state fMRI

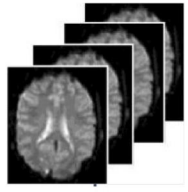

Signal

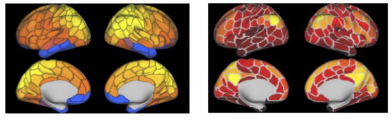

Hemodynamic response function (HRF)

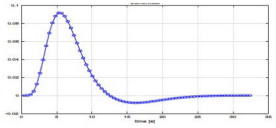

Static FC (sFC)

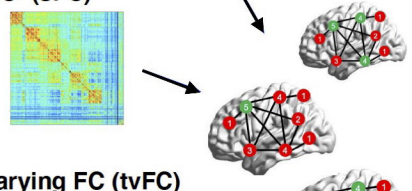

Time-varying FC (tvFC)

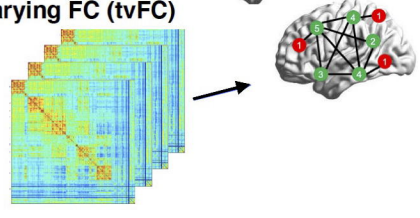

## [18F]FDG PET

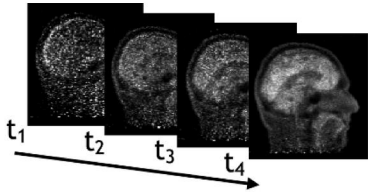


Compartment modeling

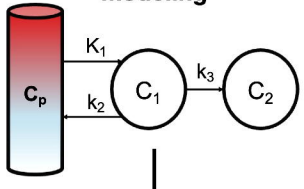


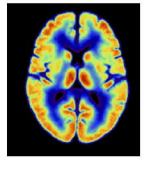

$K_i$
[ml/cm$^3$/min]

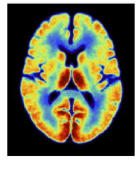

$K_1$
[ml/cm$^3$/min]

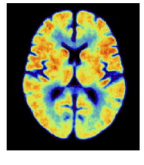

$k_3$
[min$^{-1}$]

## $^{15}$O PET

Compartment modeling

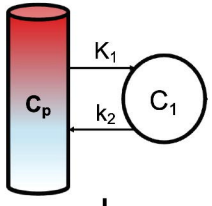


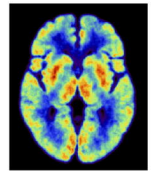

**CBF**
[ml/cm$^3$/min]

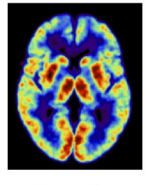

**$CMRO_2$**
[ml/cm$^3$/min]

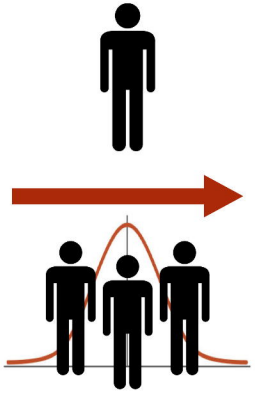

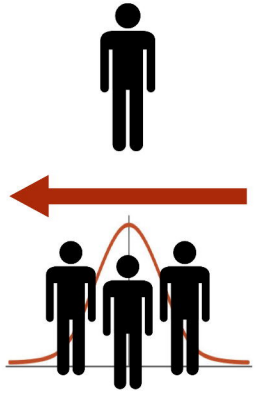

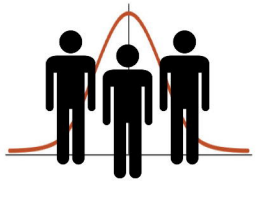

**Bivariate Correlation**
**&**
**Multivariable Multilevel Modeling**

$K_i$ [mL/cm$^3$/min]

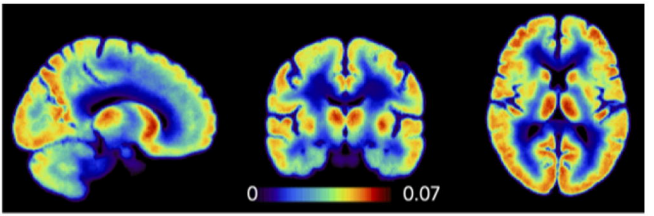


$K_1$ [mL/cm$^3$/min]

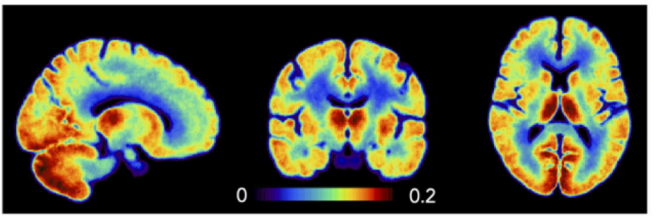


$k_3$ [min$^{-1}$]

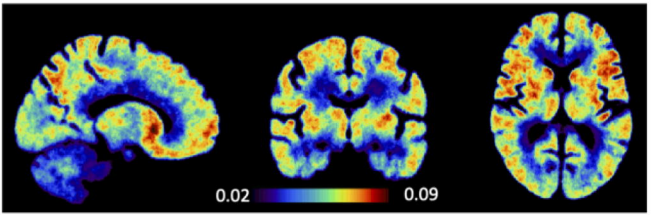

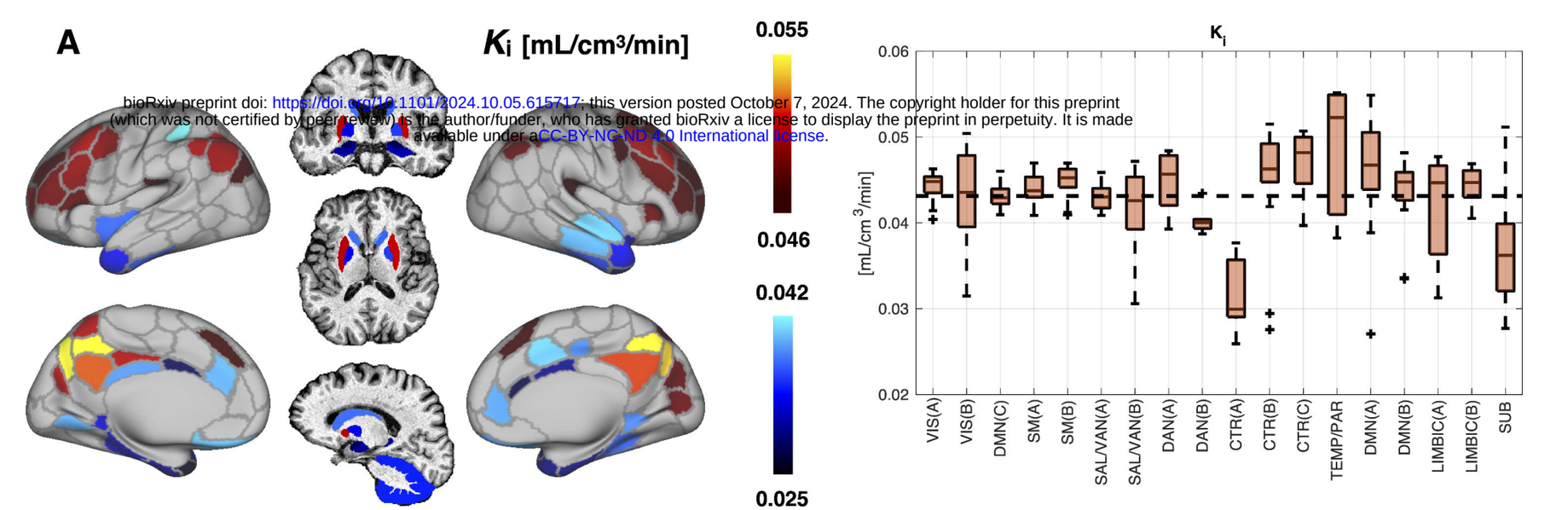


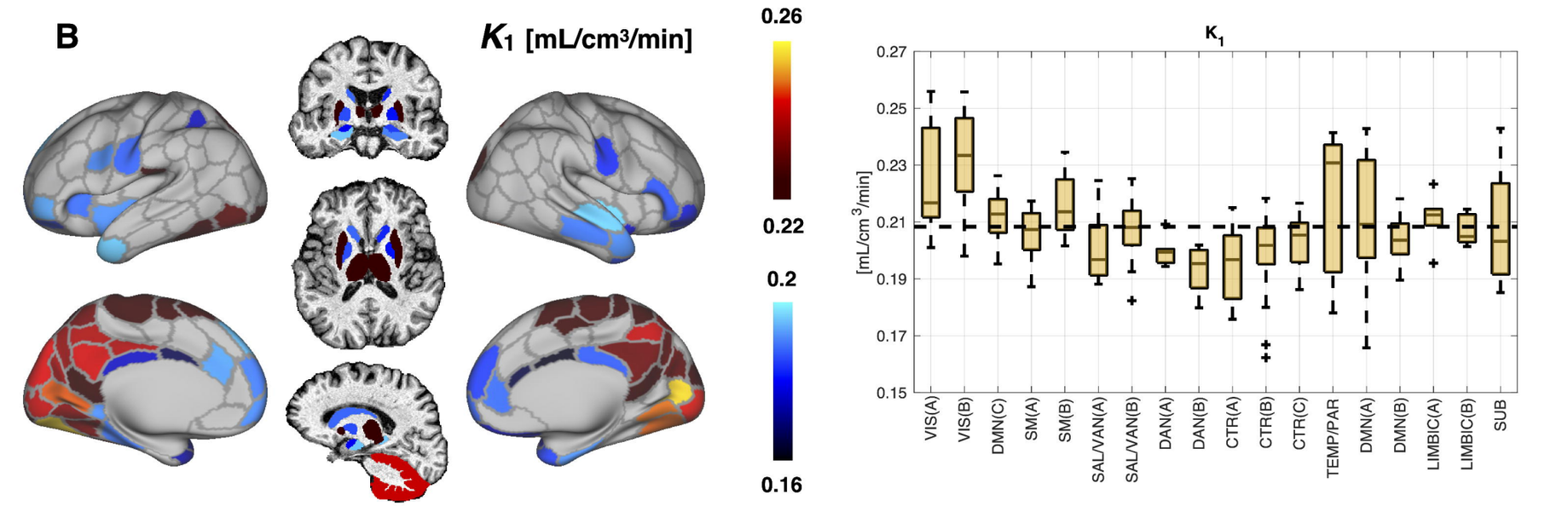


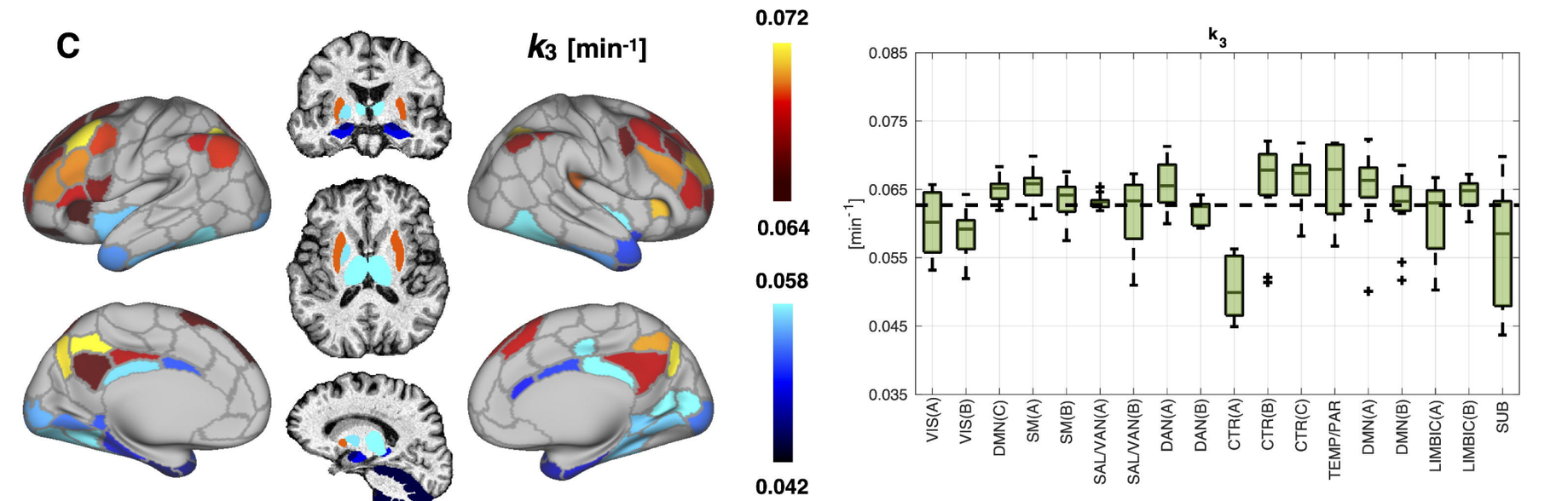

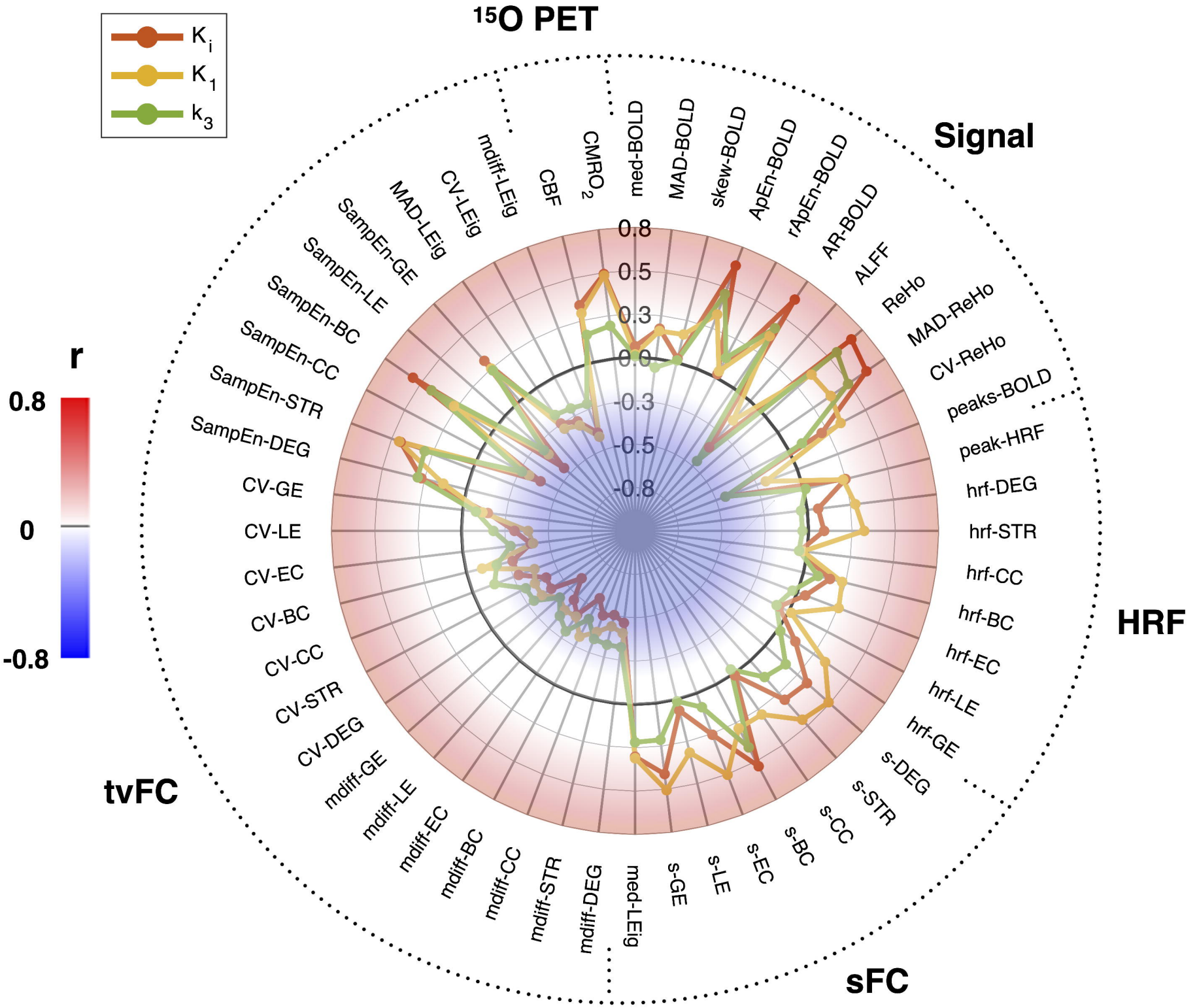
$K_i$
$K_1$
$k_3$
$^{15}O$ PET
Signal
HRF
sFC
tvFC
r
0.8
0
-0.8
0.8
0.5
0.3
0.0
-0.3
-0.5
-0.8
CBF
$CMRO_2$
med-BOLD
MAD-BOLD
skew-BOLD
ApEn-BOLD
rApEn-BOLD
AR-BOLD
ALFF
ReHo
MAD-ReHo
CV-ReHo
peaks-BOLD
peak-HRF
hrf-DEG
hrf-STR
hrf-CC
hrf-BC
hrf-EC
hrf-LE
hrf-GE
s-DEG
s-STR
s-CC
s-BC
s-EC
s-LE
s-GE
med-LEig
mdiff-DEG
mdiff-STR
mdiff-CC
mdiff-BC
mdiff-EC
mdiff-LE
mdiff-GE
CV-DEG
CV-STR
CV-CC
CV-BC
CV-EC
CV-LE
CV-GE
SampEn-DEG
SampEn-STR
SampEn-CC
SampEn-BC
SampEn-LE
SampEn-GE
MAD-LEig
CV-LEig
mdiff-LEig